

NASA
TP
1497
c.1

NASA Technical Paper 1497

LOAN COPY RETURN TO
AFWL TECHNICAL LIBRARY
KIRTLAND AFB, N. M.



A Hybridized Method for Computing High-Reynolds-Number Hypersonic Flow About Blunt Bodies

K. James Weilmuenster and H. Harris Hamilton II

OCTOBER 1979

NASA



NASA Technical Paper 1497

A Hybridized Method for Computing High-Reynolds-Number Hypersonic Flow About Blunt Bodies

K. James Weilmuenster and H. Harris Hamilton II
Langley Research Center
Hampton, Virginia

NASA

National Aeronautics
and Space Administration

**Scientific and Technical
Information Branch**

1979

SUMMARY

A hybridized method for computing the flow about blunt bodies is presented. In this method, the flow field is split into its viscid and inviscid parts.

The forebody flow field about a parabolic body is computed. For the viscous solution, the Navier-Stokes equations are solved on orthogonal parabolic coordinates using explicit finite differencing. The inviscid flow is determined by using a "Moretti type" scheme in which the Euler equations are solved, using explicit finite differences, on a nonorthogonal coordinate system which uses the bow shock as an outer boundary. The two solutions are coupled along a common data line and are marched together in time until a converged solution is obtained.

Computed results, when compared with experimental and analytical results, indicate the method works well over a wide range of Reynolds numbers and Mach numbers.

INTRODUCTION

Over a number of years, highly refined techniques have been developed for obtaining flow-field solutions about blunt entry bodies at supersonic and hypersonic speeds. Early techniques included the inviscid shock-layer method of Moretti and Salas (ref. 1) and the viscous shock-layer method of Davis (ref. 2) and others. The more recent work of Kumar (ref. 3) has extended viscous blunt-body calculations to include solutions for small angles of attack and for the plane of symmetry. In one way or another, all of these methods use a coordinate system tied to the body shape along with a transformation of the physical space into a uniform rectangular mesh in the computational plane. The dependence of the transformations on body shape necessarily limits these techniques to flow over smooth shapes, since any attempt to carry the solutions past a sharp forebody/afterbody juncture will result in a singularity in the coordinate transformation.

The ability to compute the complete flow field about a finite entry body has always been a desirable but, until recently, unrealized goal due largely to inadequate computer resources. Recently, Peyret and Viviani (ref. 4) and Gnoffo (ref. 5) have solved the complete flow about finite analytical bodies at an angle of attack of zero degrees. In both papers, Navier-Stokes solutions were obtained on a physical mesh which is tied to the body shape. The solution of Peyret and Viviani is for a body having a sharp forebody/afterbody juncture, while Gnoffo uses a smooth, analytical body shape. Both methods also use shock capturing to handle the bow shock. The shock capturing technique works well for flows at low Reynolds numbers. However, at high Reynolds numbers, the number of mesh points required to adequately resolve the shock are prohibitive. Gnoffo, in unpublished work at NASA Langley Research Center (LaRC), has floated a

discrete shock in his mesh to handle these conditions at high Reynolds numbers while solving the full Navier-Stokes equations everywhere in the flow field.

In this paper, we will demonstrate a technique which simultaneously solves for the flow in the inner, viscid region and the outer, inviscid region about the forebody of an axisymmetric parabola at 0° angle of attack. This technique, which is directly applicable to the finite body problem, will minimize the number of grid points required in the computational domain. Solutions for the outer, inviscid region are found using a "Moretti type" method which is tied to an arbitrary line through the flow field rather than to the body surface. The inner, viscous solution is found by solving the full Navier-Stokes equations over a region bounded by the body surface and the lower bound of the inviscid solution. The solution technique has been structured for the Control Data STAR-100 computer at Langley Research Center (ref. 6), thus, the method will be explicit in nature.

SYMBOLS

a	local speed of sound, \hat{a}/\hat{U}_∞
A	constant in equation (2)
\hat{c}_p	specific heat at constant pressure
\hat{c}_v	specific heat at constant volume
C_1	$= \hat{u}_\infty^2 / 2\hat{c}_v\hat{T}_\infty$
C_2	$= \hat{u}_\infty^2 / \hat{c}_v\hat{T}_\infty$
e	internal energy, $\hat{e}/(\hat{c}_v\hat{T}_\infty)$
$\vec{F}, \vec{G}, \vec{H}, \vec{S}, \vec{W}$	vectors defined in equations (A7)
h	$= (\xi^2 + \eta^2)^{1/2} / L^{1/2}$
I	static enthalpy, $\hat{I}/(\hat{c}_p\hat{T}_\infty)$
K	thermal conductivity, \hat{K}/\hat{K}_∞
L	reference length
M	Mach number
N_{Pr_∞}	free-stream Prandtl number, $\hat{u}_\infty\hat{c}_p/\hat{K}_\infty$
N_{Re_∞}	free-stream Reynolds number, $\hat{\rho}_\infty\hat{U}_\infty\hat{L}/\hat{\mu}_\infty$
P	pressure, $\hat{P}/(\hat{\rho}_\infty\hat{U}_\infty^2)$

q_w	wall heat transfer, $\frac{\hat{K} \frac{\partial \hat{T}}{\partial \hat{\eta}}}{\hat{\rho}_\infty \hat{U}_\infty^3}$
r_n	nose radius
s	body surface length
t	time, $\hat{t} \hat{U}_\infty / \hat{L}$
T	temperature, \hat{T} / \hat{T}_∞
u	velocity, $\hat{u} / \hat{U}_\infty \hat{L}^{1/2}$ (eq. (A3))
U	x-component of velocity
u	η -component of velocity
v	velocity, $\hat{v} / \hat{U}_\infty \hat{L}^{1/2}$ (eq. (A3))
V	y-component of velocity
V	ξ -component of velocity
x	Cartesian coordinate direction
y	Cartesian coordinate direction
γ	ratio of specific heats
Δ	increment of length
$\Delta \tilde{\eta}$	$= \eta_{\max} - \eta_0$
η	parabolic coordinate
λ	computational step size, $\Delta t / \Delta$
μ	viscosity, $\hat{\mu} / \hat{\mu}_\infty$
ξ	parabolic coordinate
ρ	density, $\hat{\rho} / \hat{\rho}_\infty$
ϕ	transformed coordinate

Subscripts:

c	common
n	normal to shock

- o reference to body surface
- s reference to post-shock conditions
- t = $\partial(\)/\partial t$
- w wall
- η = $\partial(\)/\partial \eta$
- ξ = $\partial(\)/\partial \xi$
- ∞ reference to free-stream conditions

Other notations:

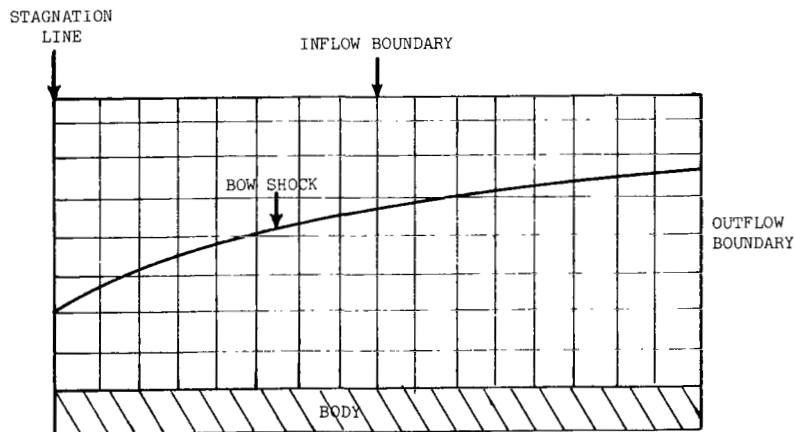
Arrow over symbol (e.g., \vec{F}) denotes vector.

Bar over symbol (e.g., \bar{t}) denotes coordinate in inviscid flow field.

Circumflex over symbol (e.g., \hat{u}) denotes dimensional variable.

ANALYSIS

Several factors were taken into account while determining the appropriate coordinate system to be used with the computational technique described in this paper. The shock capturing technique was not considered because of the large number of grid points required to adequately resolve the bow shock at the high Reynolds numbers of interest. Also, the shock floating technique was not considered because it requires a surplus of mesh points in the computational field as illustrated in the following sketch and because the logic required to float the bow shock in the grid would nullify the computational advantages of vector processing. Thus, it was determined that the physical plane to be covered should be an envelope bounded by the bow shock, the body, the outflow boundary, and the stagnation line as shown:



Rectangular Computational Plane

The global coordinate system consists of two distinct but interdependent local coordinate systems. Both systems are constructed so that, through a coordinate transformation, the numerical computations are carried out on a uniform rectangular mesh.

Local Coordinate System for the Viscous Region

The physical coordinate system used in the viscous computations is the orthogonal parabolic system used by Peyret and Viviand (ref. 4) and is formed by the intersection of curves belonging to two cofocal parabolas as shown in figure 1(a). The parametric equations for the Cartesian coordinates in this system are

$$\left. \begin{aligned} x &= \frac{1}{2}(\xi^2 - \eta^2) \\ y &= \xi\eta \end{aligned} \right\} \quad (1)$$

As seen in figure 1(b), the axisymmetric body surface is formed by rotating one of the coordinate lines, specified by a constant value of $\eta = \eta_0$, about the x-axis.

The computational technique, to be described in the section "Viscous Solution," requires a mesh ratio of one in the computational plane. Shown in figure 1(c) is the physical plane transformed to the uniform computational plane which is divided into equal increments of ξ and η (i.e., $\Delta\xi = \Delta\eta$). The mesh in the physical plane expands naturally in both the ξ - and η -directions and provides the greatest spatial resolution in the region of the nose in both the ξ - and η -directions and along the wall in the η -direction. Since the size of the viscous region for any given conditions is fixed, the spatial resolution can be controlled by either increasing or decreasing the incremental size of ξ and η which either decreases or increases the number of grid points. Controlling the resolution in this manner is sufficient when working at low Reynolds numbers, but it is inadequate at high Reynolds numbers because of the large number of grid points needed when very small values of $\Delta\eta$ are needed near the wall. The problem was overcome by applying a Blottner (ref. 7) type transformation to the η -coordinate in the form

$$\eta = \Delta\tilde{\eta} \left(\frac{A^{\chi/\Delta\chi} - 1}{\chi_{\max}/\Delta\chi - 1} \right) + \eta_0 \quad (2)$$

Now, computations are performed in the χ, ξ grid where $\Delta\chi = \Delta\xi$. This allows reasonable values of $\Delta\xi$ to be chosen while the proper distribution of points in the η -direction is controlled by χ_{\max} , $\Delta\tilde{\eta}$, and the choice of the constant A. The stretched ξ, η grid is shown in figure 1(d).

Local Coordinate System for Inviscid Region

The coordinate system used for the inviscid computation is similar to that used by Moretti and Salas (ref. 1) except that here the lower boundary of the grid system is tied to a line of constant η (the common line η_c in fig. 1(b)) rather than to the body surface. A new set of transformed coordinates $(\bar{\xi}, \bar{\eta}, \bar{t})$ is defined by the transformation equations

$$\left. \begin{aligned} \bar{\xi} &= \xi \\ \bar{\eta} &= \frac{\eta - \eta_c}{\eta_s(\xi, t) - \eta_c} \\ \bar{t} &= t \end{aligned} \right\} \quad (3)$$

which transform the region between the common line η_c and the shock wave, $\eta_s = \eta_s(\bar{\xi}, \bar{t})$, into a rectangular region with the shock forming the outer boundary. (See fig. 2.) The grid spacing in the $\bar{\xi}$ -direction and the time \bar{t} are the same for the inviscid and viscous regions. However, the coordinate system in the inviscid region is nonorthogonal because of the transformation used for $\bar{\eta}$, and since the shock location varies with time (until steady state is reached), the coordinate system also varies with time.

The Global Coordinate System

As illustrated in figure 3, the two meshes in the physical plane are joined along a constant grid line, $\eta = \eta_c$. Information along this line is computed by the viscous portion of the code and serves as a boundary condition for the inviscid portion of the code. Data on the outer boundary of the viscous solution, $\eta = \eta_{\text{interpolated}}$, are found by interpolating along lines of constant ξ in the inviscid solution. The way in which the flow field is divided into an inner and outer solution will be discussed in a later section.

Computations are carried out using velocities in the parabolic rather than Cartesian system as shown in figure 4. The physical velocities along $\xi = \text{constant}$ and $\eta = \text{constant}$ are as follows:

$$u = \frac{-\eta U + \xi V}{h} \quad (4)$$

$$v = \frac{\xi U + \eta V}{h} \quad (5)$$

Now, set $h = h_1 = h_2 = (\xi^2 + \eta^2)^{1/2}$ and define a set of coinvariant velocities

$$u = hU \quad \text{and} \quad v = hV \quad (6)$$

The use of these coinvariant velocities in the governing equations eliminates errors caused by the differencing of nonlinear metric coefficients.

Viscous Solution

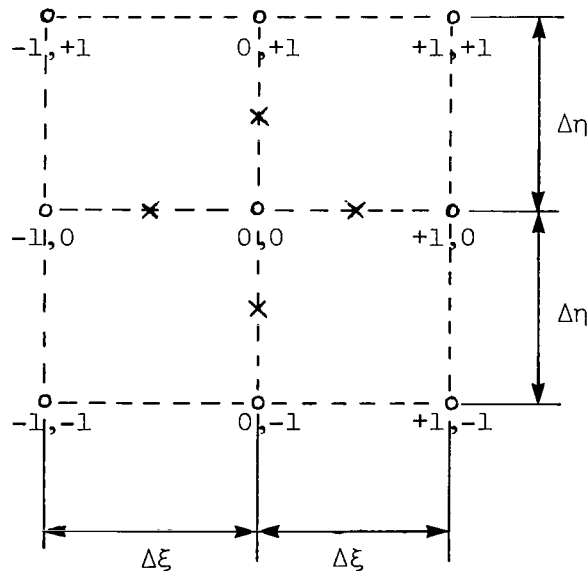
The solution in the viscous portion of the flow is obtained by integrating the full, compressible, time-dependent Navier-Stokes equations on the orthogonal parabolic grid described in the previous section. The integration is carried out by applying a modified version of the two-step Richtmeyer differencing algorithm described by Thommen in reference 8 to the appropriate system of equations.

The governing equations are written in the conservative form

$$\vec{W}_t = - \frac{\partial \vec{F}(W)}{\partial \xi} - \frac{\partial \vec{G}(W)}{\partial \eta} + \vec{H}(W) + \vec{S}(W) \quad (7)$$

where the terms in equation (7) are the conserved quantities \vec{W} , the convective terms \vec{F} and \vec{G} , the geometry terms \vec{H} arising from a non-Cartesian coordinate system, and the viscous dissipation and heat conduction terms \vec{S} . The specific form of the Navier-Stokes equations used for this two-dimensional, axisymmetric flow in an orthogonal parabolic coordinate system is developed in appendix A.

The difference algorithm in equations (8) and (9) is used to integrate equation (7) on a nine point computational module for any W . The variable W is defined in the time plane t at the grid points represented by circles and in the plane $t + \Delta t/2$ at the points marked by crosses in this sketch:



The two-step differencing scheme is written as follows:

$$\begin{aligned} \vec{W}_{\pm 1/2,0}^{\rightarrow t+\Delta t/2} &= \frac{1}{2}(\vec{W}_{\pm 1,0}^{\rightarrow t} + \vec{W}_{0,0}^{\rightarrow t}) - \frac{\Delta t}{2} \left[\langle \vec{F}_{\xi} \rangle_{\pm 1/2,0}^t + \langle \vec{G}_{\eta} \rangle_{\pm 1/2,0}^t \right. \\ &\quad \left. - \frac{1}{2}(\vec{H}_{\pm 1,0}^{\rightarrow t} + \vec{H}_{0,0}^{\rightarrow t}) - \frac{1}{2}(\vec{S}_{\pm 1,0}^{\rightarrow t} + \vec{S}_{0,0}^{\rightarrow t}) \right] \end{aligned} \quad (8a)$$

$$\begin{aligned} \vec{W}_{0,\pm 1/2}^{\rightarrow t+\Delta t/2} &= \frac{1}{2}(\vec{W}_{0,\pm 1}^{\rightarrow t} + \vec{W}_{0,0}^{\rightarrow t}) - \frac{\Delta t}{2} \left[\langle \vec{F}_{\xi} \rangle_{0,\pm 1/2}^t + \langle \vec{G}_{\eta} \rangle_{0,\pm 1/2}^t \right. \\ &\quad \left. - \frac{1}{2}(\vec{H}_{1,\pm 1}^{\rightarrow t} + \vec{H}_{0,0}^{\rightarrow t}) - \frac{1}{2}(\vec{S}_{0,\pm 1}^{\rightarrow t} + \vec{S}_{0,0}^{\rightarrow t}) \right] \end{aligned} \quad (8b)$$

$$\vec{W}_{0,0}^{\rightarrow t+\Delta t} = \vec{W}_{0,0}^{\rightarrow t} - \Delta t \left(\langle \vec{F}_{\xi} \rangle_{0,0}^{t+\Delta t/2} + \langle \vec{G}_{\eta} \rangle_{0,0}^{t+\Delta t/2} - \vec{H}_{0,0}^{\rightarrow t} - \vec{S}_{0,0}^{\rightarrow t} \right) \quad (9)$$

The first-order functions in equations (8) and (9) can be written for either \vec{F} or \vec{G} as

$$\left. \begin{aligned} \langle \vec{F}_{\xi} \rangle_{\pm 1/2,0}^t &= \pm \frac{1}{\Delta \xi} (\vec{F}_{\pm 1,0}^{\rightarrow t} - \vec{F}_{0,0}^{\rightarrow t}) \\ \langle \vec{F}_{\eta} \rangle_{\pm 1/2,0}^t &= \frac{1}{4\Delta \eta} (\vec{F}_{0,+1}^{\rightarrow t} + \vec{F}_{\pm 1,+1}^{\rightarrow t} - \vec{F}_{0,-1}^{\rightarrow t} - \vec{F}_{\pm 1,-1}^{\rightarrow t}) \\ \langle \vec{F}_{\xi} \rangle_{0,0}^{t+\Delta t/2} &= \frac{1}{\Delta \xi} (\vec{F}_{+1/2,0}^{\rightarrow t+\Delta t/2} - \vec{F}_{-1/2,0}^{\rightarrow t+\Delta t/2}) \end{aligned} \right\} \quad (10)$$

Their counterparts $\langle \vec{G}_{\xi} \rangle_{0,\pm 1/2}^t$, $\langle \vec{G}_{\eta} \rangle_{0,\pm 1/2}^t$, and $\langle \vec{G}_{\eta} \rangle_{0,0}^{t+\Delta t/2}$ are found by permuting indices in equations (10). The second derivatives used in the viscous term \vec{S} are defined below for the general variable ψ :

$$\left. \begin{aligned}
\langle (b\psi_\xi)_\xi \rangle_{0,0}^t &= \frac{1}{\Delta\xi^2} \left[b_{+1/2,0}^t (\psi_{+1,0}^t - \psi_{0,0}^t) - b_{-1/2,0}^t (\psi_{0,0}^t - \psi_{-1,0}^t) \right] \\
\langle (b\psi_\xi)_\eta \rangle_{0,0}^t &= \frac{1}{4\Delta\xi\Delta\eta} \left[b_{0,+1/2}^t (\psi_{+1,0}^t + \psi_{+1,+1}^t - \psi_{-1,0}^t - \psi_{-1,+1}^t) \right. \\
&\quad \left. - b_{0,-1/2}^t (\psi_{+1,0}^t + \psi_{+1,-1}^t - \psi_{-1,0}^t - \psi_{-1,-1}^t) \right] \\
b_{\pm 1/2,0}^t &= \frac{1}{2} b_{0,0}^t + b_{\pm 1,0}^t
\end{aligned} \right\} \quad (11)$$

Thommen first recommended that the \vec{H} and \vec{S} vectors be reevaluated at $t + \Delta t/2$. He later found this was unnecessary for \vec{S} . Because of the large variation of the metric coefficients near the stagnation line for this particular coordinate system, we have obtained better results in the stagnation region by not reevaluating \vec{H} .

Inviscid Solution

The solution in the inviscid portion of the flow is obtained by integrating the compressible, time-dependent Euler equations in the transformed coordinate system described in a preceding section. The integration is carried out using the two-step MacCormack finite-difference algorithm (ref. 9) which is modified by using one-sided differences at the shock boundary.

The conservative, vector form of the Euler equations written in orthogonal parabolic coordinates (ξ, η, t) is

$$\vec{W}_t = -\vec{F}_\xi(\vec{W}) - \vec{G}_\eta(\vec{W}) + \vec{H}(\vec{W}) \quad (12)$$

where \vec{W} , \vec{F} , \vec{G} , and \vec{H} are the same vector quantities defined in appendix A. By using the transformation equations (eqs. (3)), the system of equations (eq. (12)) can be transformed from parabolic coordinates (ξ, η, t) to a set of coordinates in the computational space $(\bar{\xi}, \bar{\eta}, \bar{t})$. Thus, equation (12) becomes

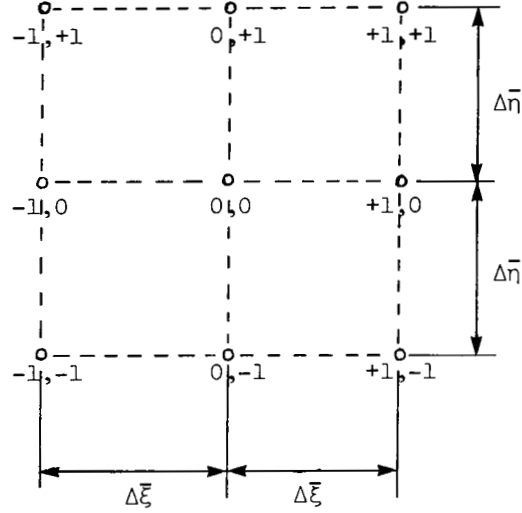
$$\vec{W}_{\bar{t}} = -\frac{\partial \bar{\eta}}{\partial \bar{t}} \vec{W}_{\bar{\eta}} - \vec{F}_{\bar{\xi}} - \frac{\partial \bar{\eta}}{\partial \bar{\xi}} \vec{F}_{\bar{\eta}} - \frac{\partial \bar{\eta}}{\partial \bar{\eta}} \vec{G}_{\bar{\eta}} + \vec{H} \quad (13)$$

Since only the steady-state solution is of interest, the term $\frac{\partial \bar{\eta}}{\partial \bar{t}} \vec{W}_{\bar{\eta}}$ is neglected and equation (13) becomes

$$\vec{w}_t = -\vec{F}_\xi - \frac{\partial \bar{\eta}}{\partial \xi} \vec{F}_\eta - \frac{\partial \bar{\eta}}{\partial \eta} \vec{G}_\eta + \vec{H} \quad (14)$$

The details of this transformation are given in appendix B.

The difference algorithm in equations (15) and (16) is used to integrate equation (14) on the computational module illustrated below:



The variable \vec{w} is defined in the plane $t = 0$ at the points represented by the circles in the sketch above. The two-step MacCormack difference scheme is then written as follows for the solution of \vec{w} at the time plane $t + \Delta t$:

Predictor step -

$$\begin{aligned} \overline{\vec{w}}_{0,0}^{t+\Delta t} = & \vec{w}_{0,0}^t - \Delta t \left[\left(\frac{\partial \vec{F}}{\partial \xi} \right)_{0,0}^t + \left(\frac{\partial \bar{\eta}}{\partial \xi} \right)_{0,0}^t \left(\frac{\partial \vec{F}}{\partial \bar{\eta}} \right)_{0,0}^t \right. \\ & \left. + \left(\frac{\partial \bar{\eta}}{\partial \eta} \right)_{0,0}^t \left(\frac{\partial \vec{G}}{\partial \bar{\eta}} \right)_{0,0}^t - (\vec{H})_{0,0}^t \right] \end{aligned} \quad (15)$$

Corrector step -

$$\begin{aligned} \vec{w}_{0,0}^{t+\Delta t} = & \frac{1}{2} \left\{ \vec{w}_{0,0}^t + \overline{\vec{w}}_{0,0}^{t+\Delta t} - \Delta t \left[\left(\frac{\partial \vec{F}}{\partial \xi} \right)_{0,0}^{t+\Delta t} + \left(\frac{\partial \bar{\eta}}{\partial \xi} \right)_{0,0}^{t+\Delta t} \left(\frac{\partial \vec{F}}{\partial \bar{\eta}} \right)_{0,0}^{t+\Delta t} \right. \right. \\ & \left. \left. + \left(\frac{\partial \bar{\eta}}{\partial \eta} \right)_{0,0}^{t+\Delta t} \left(\frac{\partial \vec{G}}{\partial \bar{\eta}} \right)_{0,0}^{t+\Delta t} - (\vec{H})_{0,0}^{t+\Delta t} \right] \right\} \end{aligned} \quad (16)$$

At the interior points on the computational grid, two-point backward differences are used to replace the derivatives of \vec{F} and \vec{G} in the predictor step and two-point forward differences are used in the corrector step. For the grid points along the bow shock, three-point backward differences are used in both the predictor and corrector steps. The procedure used to track the movement of the bow shock wave will be described in the next section.

Solution for Shock Wave

A method similar to that used by Tannehill, Holst, and Rakich (ref. 10) has been used to track the movement of the shock wave during the transient portion of the solution. The method can be summarized as follows (details are given in appendix C). First, the pressure is computed on the downstream side of the shock wave using the two-step difference scheme described in the preceding section with three-point backward differences used to compute $\partial\vec{F}/\partial\vec{\eta}$ and $\partial\vec{G}/\partial\vec{\eta}$ at the shock wave. With the pressure at the shock wave P_S known, the density is computed using the equation

$$\frac{1}{\rho_S} = \left[\frac{\frac{\gamma I_\infty}{C_2} + \frac{1}{2}(P_S - P_\infty)}{P_S \left(\frac{C_2}{\gamma - 1} \right) - \frac{1}{2}(P_S - P_\infty)} \right] \quad (17)$$

Then, the shock velocity is computed using the equation

$$V_S = (V_n)_\infty \sqrt{\frac{P_S - P_\infty}{1 - \frac{1}{\rho_S}}} \quad (18)$$

where V_S and $(V_n)_\infty$ are defined in sketches (c) and (b) in appendix C.

Next, the movement of the shock wave (see fig. 5) is computed using the following two-step difference method:

Predictor step -

$$(\eta_S)^{\overline{t+\Delta t}} = (\eta_S)^t - \Delta t \left(\frac{V_S}{h \cos \zeta_S} \right)^t \quad (19)$$

Corrector step -

$$(\eta_S)^{t+\Delta t} = (\eta_S)^t - \frac{\Delta t}{2} \left[\left(\frac{V_S}{h \cos \zeta_S} \right)^t + \left(\frac{V_S}{h \cos \zeta_S} \right)^{\overline{t+\Delta t}} \right] \quad (20)$$

where

$$\zeta_s = \tan^{-1} \left(\frac{\partial \eta_s}{\partial \xi} \right) \quad (21)$$

The derivative $\partial \eta_s / \partial \xi$ in equation (21) is approximated by central differences in both the predictor and corrector steps. After the new location of the shock wave has been determined, the properties (except pressure) on the downstream side of the shock are computed using a transient shock-wave analysis.

As the solution approaches convergence, the shock velocity approaches zero and the shock wave remains essentially fixed in space. This usually occurs before the remaining properties in the flow field converge. The shock velocities at convergence are generally less than 10^{-4} in magnitude.

BOUNDARY AND INITIAL CONDITIONS

Boundary Conditions

Viscous region.- Along the body surface, the usual no-slip boundary conditions, $u = 0$ and $v = 0$, are imposed. Wall pressure is found by setting the normal pressure gradient $\partial P / \partial \eta$ equal to zero while the wall temperature is held constant at some predetermined value. Thus, the wall density is found from the equation of state.

Symmetry conditions

$$\left. \begin{aligned} \rho(\eta, -\Delta\xi) &= \rho(\eta, \Delta\xi) \\ u(\eta, -\Delta\xi) &= u(\eta, \Delta\xi) \\ v(\eta, -\Delta\xi) &= -v(\eta, \Delta\xi) \\ e(\eta, -\Delta\xi) &= e(\eta, \Delta\xi) \\ P(\eta, -\Delta\xi) &= P(\eta, \Delta\xi) \end{aligned} \right\} \quad (22)$$

are imposed along the stagnation line $\xi = 0$. At the outflow boundary, a second-order extrapolation of the conserved variables

$$\vec{W}(\xi_{\max}, \eta) = 3\vec{W}(\xi_{\max} - \Delta\xi, \eta) - 3\vec{W}(\xi_{\max} - 2\Delta\xi, \eta) + \vec{W}(\xi_{\max} - 3\Delta\xi, \eta) \quad (23)$$

is used.

As shown in figure 3, the inflow boundary for the viscous solution is determined by linearly interpolating along lines of constant ξ on information in the inviscid solution to get values along $\eta = \eta_{\text{interpolated}}$.

Inviscid solution.- As shown in figure 3, the lower boundary of the inviscid solution is fixed by making it coincident with the line $\eta = \eta_c$, the last line of computed information in the viscous solution. Along the stagnation line, the symmetry conditions are the same as those used in the viscous solution.

Values along the outflow boundary are determined by a second-order extrapolation of values at the interior points, while the values on the inflow boundary are determined by the unsteady shock relations discussed in the inviscid flow section.

Initial conditions.- Initial conditions are imposed in the following manner. The wall surface temperature is fixed and velocities at the wall are set equal to zero while a Newtonian pressure distribution is determined for the given body shape. An initial shock shape, which is usually a line of constant η , is picked. Steady shock relations are then used to determine flow conditions behind the shock. The pressure and velocities are then linearly interpolated between the shock and body along lines of constant ξ . Finally, the temperature along each line of constant ξ is set equal to the shock temperature up to, but not including, the wall. The density distribution is then found using the equation of state.

Numerical Stability

The inviscid numerical stability limit for the two methods being used is the well-known CFL condition

$$\Delta t = \frac{C_0/C'}{\frac{|u|}{\Delta x} + \frac{|v|}{\Delta y} + a\sqrt{\frac{1}{\Delta x} + \frac{1}{\Delta y}}} \quad (24)$$

where $C' = 1$ for the MacCormack scheme and $C' = 2$ for the Richtmeyer scheme. For both methods, the Courant number C_0 is taken to be 0.95. When equation (24) is applied to the present coordinate system and u and v are used as defined in appendix A, the equation becomes

$$\frac{\Delta t}{\Delta} = \frac{(C_0/C')h^2}{|u| + |v| + \sqrt{2} ha} \quad (25)$$

and, when the Blottner coordinate transformation is applied to the viscous equations,

$$\frac{\Delta t}{\Delta} = \frac{(C_0/C')h^2}{(|u| + |v| + \sqrt{2} ha) \frac{\partial \eta}{\partial \phi}} \quad (26)$$

The viscous stability limit for the Richtmeyer scheme is

$$\frac{\Delta t}{\Delta} = \frac{\rho}{\mu} N_{Re_\infty} \Delta$$

and for the Blottner transformation is

$$\frac{\Delta t}{\Delta} = \frac{\rho}{\mu \left(\frac{\partial \eta}{\partial \phi} \right)^2} N_{Re_\infty} \Delta$$

Global Operational Characteristics

The preceding procedure has been programed and run on the Control Data STAR-100 computer at Langley Research Center. The computational mesh size used depends on the flow Reynolds number and on the need to adjust the relative position of points in the two meshes. Inviscid mesh size varied from 6×21 to 12×21 , and the viscous mesh varied from 14×21 to 25×21 . Normal mesh spacing in the viscous region was determined by requiring that the stagnation-point cell Reynolds number equal two.

Initially, solutions were obtained using a single value of Δt which was determined by finding the minimum of all local values of Δt . However, the combination of a high Reynolds number with the restriction on cell Reynolds number led to extremely small values of Δt near the wall. This led us to try using the local minimum Δt at each point, as reported by Kumar (ref. 3). This procedure yielded good results and gave us a reduction of approximately 50 percent in the number of iterations required to reach convergence for the highest Reynolds number runs.

The actual running of a computer code as described always raises a number of operational problems which cannot be quantified. In particular, a number of problems have appeared at the juncture of the inviscid and viscous flow meshes. Each problem has been resolved, but for most, there is a lack of a definitive cause-and-effect relationship.

The first and most obvious problem is determining whether the flow field is properly split into its viscous and inviscid components. We quickly found that

the code simply would not run if the inviscid region extended into the viscous region. We surmounted this problem by being very conservative in our estimate of the extent of the viscous region.

We also found that, in order to maintain a stable computation, the interpolated row of data in the viscous solution must be coincident with, or have a value of η greater than, that of the second row of data in the inviscid solution.

The flow-field solution was considered to be converged when the relative convergence criterion

$$\left| \frac{\rho^{t+\Delta t} - \rho^t}{\rho^t} \right| \leq 10^{-5}$$

was satisfied at every point in the flow field.

RESULTS AND DISCUSSION

The preferred method of validating numerical techniques is comparison with experimental data. Experimental data for flow over parabolic bodies are scarce and basically limited to drag coefficients. We have used the data of Little (ref. 11) and information generated in the Langley continuous-flow hypersonic tunnel (CFHT) for drag data. Shock shapes were obtained from tests run in the Mach 6 high Reynolds number tunnel at the Langley Research Center. Also, comparisons are made with established numerical methods to determine the accuracy of pressure and heat-transfer distributions. All computations have been made using the Sutherland viscosity formula and a perfect gas with a ratio of specific heats of 1.4.

Our first concern was determining the effect of splitting the flow field on the overall accuracy of the solution (specifically, determine whether the physical joining of two different computational meshes would distort the solution in the vicinity of the juncture). To check this, we compared the complete inviscid solution with the coupled solution for two different sets of free-stream flow conditions. For the first condition, shown in figure 6, $N_{Re_\infty} = 2 \times 10^6$ and $M_\infty = 5.87$. Here, temperature profiles are plotted for the stagnation line ($\xi = 0$) and a point approximately halfway around the body. Both curves indicate a smooth transition from one mesh to the other at the point marked "mesh juncture" which is the last computed point in the viscous solution. Also, the two solutions agree very well down to the point where boundary-layer effects dominate the flow. However, there is, as expected, some difference between the two curves due to the effect of boundary-layer growth on effective body shape. The plot presented in figure 7 is similar except that the N_{Re_∞} has been reduced to 3×10^5 and $M_\infty = 9.92$. Again, good results were obtained, but the difference between the two curves at the downstream location is more pronounced due to the more rapid boundary-layer growth.

Next, a comparison is made with experimental drag coefficients. In figure 8, numerical results are compared with the data of Little (ref. 11). The present method can be used only for body configurations which have supersonic outflow boundary conditions outside of the boundary layer. There is, however, good agreement with experimental data over the range of conditions which can be duplicated by the present program. It is also interesting to note the viscous effect on the drag coefficient, even at these relatively large Reynolds numbers, as indicated by the divergence of the viscid and inviscid curves as body length increases.

The second comparison is made with experimental drag coefficients based on data taken in the Langley CFHT and is shown in figure 9. Here, the comparison of variations in the drag coefficient is made for a range of Reynolds numbers on a 30° paraboloid.

Our last comparison is made with experimental data for the shock shape shown in figure 10. The experimental shock shape was obtained from schlieren photographs taken in the Mach 6 high Reynolds number tunnel at the Langley Research Center for the conditions $M_\infty = 5.8725$ and $N_{Re_\infty} = 2 \times 10^6$. Again, there is excellent agreement between experimental and numerical results.

There is no experimental heat-transfer data available for comparison with results generated by our present method. Therefore, we have chosen to make our comparisons with the results generated by several proven computer codes. For $M_\infty = 10.34$ and $N_{Re_\infty} = 5 \times 10^5$, results are shown in figure 11. The results from the present method are compared with computations using the Navier-Stokes solution of Graves (ref. 12), the viscous shock-layer solution of Kumar (ref. 3), and the boundary-layer solution of Anderson (ref. 13) which uses the inviscid edge conditions from Marconi (ref. 14). As can be seen in figure 11, there is extremely good agreement among all methods. In figure 12, similar results are shown for the free-stream conditions $M_\infty = 5.8725$ and $N_{Re_\infty} = 2 \times 10^6$.

CONCLUDING REMARKS

In the previous sections, we have investigated the viability of a hybrid viscous/inviscid solution technique for determining the flow about an axisymmetric parabola. In this investigation, we have found that it is possible for a flow-field computation to be marched in time to convergence, where the field is split into an inviscid region governed by the Euler equations and a viscous region governed by the Navier-Stokes equations. Furthermore, we have experienced no problems at the juncture of the two flow regimes when the flow field has been properly split into its viscous and inviscid parts. By comparison with both analytical and experimental results, we have demonstrated that the technique works well over a wide range of Reynolds numbers and Mach numbers.

As presented, this technique reduces the number of grid points required in the computational field, and by its explicit nature, the method is well suited to take advantage of the high computational speed of vector processing computers.

Although presented for forebody flows only, there are no conceptual problems to extending this technique to the flow about finite, sharp-cornered bodies.

Langley Research Center
National Aeronautics and Space Administration
Hampton, VA 23665
July 6, 1979

APPENDIX A

AXISYMMETRIC NAVIER-STOKES EQUATIONS IN

ORTHOGONAL PARABOLIC COORDINATES

General Equations

The dimensional Navier-Stokes equations,¹ written in conservation form for a general, curvilinear coordinate system, may be stated in terms of the system metric coefficients, h_1 , h_2 , and h_3 , as follows:

Continuity -

$$\frac{\partial}{\partial t}(h_1 h_2 h_3 \rho) + \frac{\partial}{\partial x_1}(h_2 h_3 \rho u_1) + \frac{\partial}{\partial x_2}(h_1 h_3 \rho u_2) + \frac{\partial}{\partial x_3}(h_1 h_2 \rho u_3) = 0 \quad (\text{Ala})$$

x_1 -momentum -

$$\begin{aligned} & \frac{\partial}{\partial t}(h_1 h_2 h_3 \rho u_1) + \frac{\partial}{\partial x_1} \left[h_2 h_3 \left(P + \rho u_1^2 \right) \right] + \frac{\partial}{\partial x_2}(h_1 h_3 \rho u_1 u_2) + \frac{\partial}{\partial x_3}(h_1 h_2 \rho u_1 u_3) \\ & - \left(P + \rho u_2^2 \right) h_3 \frac{\partial h_2}{\partial x_1} + \rho u_1 u_2 h_3 \frac{\partial h_1}{\partial x_2} + \rho u_1 u_3 h_2 \frac{\partial h_1}{\partial x_3} - \left(P + \rho u_3^2 \right) h_2 \frac{\partial h_3}{\partial x_1} \\ & = \frac{\partial}{\partial x_1}(h_2 h_3 \tau_{11}) + \frac{\partial}{\partial x_2}(h_1 h_3 \tau_{21}) + \frac{\partial}{\partial x_3}(h_1 h_2 \tau_{31}) \\ & + \tau_{21} h_3 \frac{\partial h_1}{\partial x_2} + \tau_{31} h_2 \frac{\partial h_1}{\partial x_3} - \tau_{22} h_3 \frac{\partial h_2}{\partial x_1} - \tau_{33} h_2 \frac{\partial h_3}{\partial x_1} \end{aligned} \quad (\text{Alb})$$

¹For convenience, the superscript denoting dimensionality [^] has been omitted from these equations.

APPENDIX A

x_2 -momentum -

$$\begin{aligned}
 & \frac{\partial}{\partial t}(h_1 h_2 h_3 \rho u_2) + \frac{\partial}{\partial x_1}(h_2 h_3 \rho u_1 u_2) + \frac{\partial}{\partial x_2} \left[h_1 h_3 (\rho u_2^2 + P) \right] + \frac{\partial}{\partial x_3}(h_1 h_2 \rho u_2 u_3) \\
 & - (\rho u_3^2 + P) h_1 \frac{\partial h_3}{\partial x_2} + \rho u_2 u_3 h_1 \frac{\partial h_2}{\partial x_3} + \rho u_1 u_2 h_3 \frac{\partial h_2}{\partial x_1} - (\rho u_1^2 + P) h_3 \frac{\partial h_1}{\partial x_2} \\
 & = \frac{\partial}{\partial x_1}(h_2 h_3 \tau_{12}) + \frac{\partial}{\partial x_2}(h_3 h_1 \tau_{22}) + \frac{\partial}{\partial x_3}(h_1 h_2 \tau_{32}) \\
 & + \tau_{23} h_1 \frac{\partial h_2}{\partial x_3} + \tau_{12} h_3 \frac{\partial h_2}{\partial x_1} - \tau_{33} h_1 \frac{\partial h_3}{\partial x_2} - \tau_{11} h_3 \frac{\partial h_1}{\partial x_2}
 \end{aligned} \tag{A1c}$$

x_3 -momentum -

$$\begin{aligned}
 & \frac{\partial}{\partial t}(h_1 h_2 h_3 \rho u_3) + \frac{\partial}{\partial x_1}(h_2 h_3 \rho u_1 u_3) + \frac{\partial}{\partial x_2}(h_1 h_3 \rho u_2 u_3) + \frac{\partial}{\partial x_3} \left[h_1 h_2 (\rho u_3^2 + P) \right] \\
 & - (\rho u_1^2 + P) h_2 \frac{\partial h_1}{\partial x_3} + \rho u_1 u_3 h_2 \frac{\partial h_3}{\partial x_1} + \rho u_2 u_3 h_1 \frac{\partial h_3}{\partial x_2} - (\rho u_2^2 + P) h_1 \frac{\partial h_2}{\partial x_3} \\
 & = \frac{\partial}{\partial x_1}(h_2 h_3 \tau_{13}) + \frac{\partial}{\partial x_2}(h_3 h_1 \tau_{23}) + \frac{\partial}{\partial x_3}(h_1 h_2 \tau_{33}) \\
 & + \tau_{31} h_2 \frac{\partial h_3}{\partial x_1} + \tau_{23} h_1 \frac{\partial h_3}{\partial x_2} - \tau_{11} h_2 \frac{\partial h_1}{\partial x_3} - \tau_{22} h_1 \frac{\partial h_2}{\partial x_3}
 \end{aligned} \tag{A1d}$$

Energy equation -

$$\begin{aligned}
 & \frac{\partial}{\partial t}(h_1 h_2 h_3 E) + \frac{\partial}{\partial x_1} \left[h_2 h_3 u_1 (E + P) \right] + \frac{\partial}{\partial x_2} \left[h_1 h_3 u_2 (E + P) \right] + \frac{\partial}{\partial x_3} \left[h_1 h_2 u_3 (E + P) \right] \\
 & = \frac{\partial}{\partial x_1} \left(\frac{h_2 h_3}{h_1} \kappa \frac{\partial T}{\partial x_1} \right) + \frac{\partial}{\partial x_2} \left(\frac{h_1 h_3}{h_2} \kappa \frac{\partial T}{\partial x_2} \right) + \frac{\partial}{\partial x_3} \left(\frac{h_1 h_2}{h_3} \kappa \frac{\partial T}{\partial x_3} \right) \\
 & + \frac{\partial}{\partial x_1} \left[h_2 h_3 (u_1 \tau_{11} + u_2 \tau_{12} + u_3 \tau_{13}) \right] + \frac{\partial}{\partial x_2} \left[h_1 h_3 (u_1 \tau_{12} + u_2 \tau_{22} + u_3 \tau_{23}) \right] \\
 & + \frac{\partial}{\partial x_3} \left[h_1 h_2 (u_1 \tau_{13} + u_2 \tau_{23} + u_3 \tau_{33}) \right]
 \end{aligned} \tag{A1e}$$

where E is defined as $\rho \left(e + \frac{u_1^2 + u_2^2 + u_3^2}{2} \right)$. The viscous stress terms are defined as follows:

$$\tau_{11} = 2\mu \left(\frac{1}{h_1} \frac{\partial u_1}{\partial x_1} + \frac{u_2}{h_1 h_2} \frac{\partial h_1}{\partial x_2} + \frac{u_3}{h_3 h_1} \frac{\partial h_1}{\partial x_3} \right) + \lambda \nabla \cdot \vec{v}$$

where

$$\lambda \nabla \cdot \vec{v} = - \frac{2\mu}{3h_1 h_2 h_3} \left[\frac{\partial}{\partial x_1} (h_2 h_3 u_1) + \frac{\partial}{\partial x_2} (h_1 h_3 u_2) + \frac{\partial}{\partial x_3} (h_1 h_2 u_3) \right]$$

$$\tau_{22} = 2\mu \left(\frac{1}{h_2} \frac{\partial u_2}{\partial x_2} + \frac{u_3}{h_2 h_3} \frac{\partial h_2}{\partial x_3} + \frac{u_1}{h_1 h_2} \frac{\partial h_2}{\partial x_1} \right) + \lambda \nabla \cdot \vec{v}$$

$$\tau_{33} = 2\mu \left(\frac{1}{h_3} \frac{\partial u_3}{\partial x_3} + \frac{u_1}{h_3 h_1} \frac{\partial h_3}{\partial x_1} + \frac{u_2}{h_2 h_3} \frac{\partial h_3}{\partial x_2} \right) + \lambda \nabla \cdot \vec{v}$$

$$\tau_{23} = \mu \left[\frac{h_3}{h_2} \frac{\partial}{\partial x_2} \left(\frac{u_3}{h_3} \right) + \frac{h_2}{h_3} \frac{\partial}{\partial x_3} \left(\frac{u_2}{h_2} \right) \right]$$

$$\tau_{13} = \mu \left[\frac{h_1}{h_3} \frac{\partial}{\partial x_3} \left(\frac{u_1}{h_1} \right) + \frac{h_3}{h_1} \frac{\partial}{\partial x_1} \left(\frac{u_3}{h_3} \right) \right]$$

$$\tau_{12} = \mu \left[\frac{h_2}{h_1} \frac{\partial}{\partial x_1} \left(\frac{u_2}{h_2} \right) + \frac{h_1}{h_2} \frac{\partial}{\partial x_2} \left(\frac{u_1}{h_1} \right) \right]$$

$$\tau_{21} = \tau_{12}$$

$$\tau_{31} = \tau_{13}$$

$$\tau_{32} = \tau_{23}$$

Equations in Parabolic Coordinates

For the orthogonal parabolic coordinate system, the following substitutions are made in equations (A1):

APPENDIX A

$$x_1 = \xi$$

$$x_2 = \eta$$

$$x_3 = \phi$$

$$u_1 = V$$

$$u_2 = U$$

$$u_3 = W$$

$$h_1 = (\xi^2 + \eta^2)^{1/2}$$

$$h_2 = (\xi^2 + \eta^2)^{1/2}$$

$$h_3 = \xi\eta$$

Furthermore, W and $\partial/\partial\phi$ are set equal to zero for axisymmetric flow. These substitutions and restrictions, when applied to the general equations, lead to the following set of equations:

Continuity equation -

$$\frac{\partial}{\partial t}(h_1 h_2 h_3 \rho) + \frac{\partial}{\partial \xi}(h_2 h_3 \rho V) + \frac{\partial}{\partial \eta}(h_1 h_3 \rho U) = 0 \quad (\text{A2a})$$

ξ -momentum equation -

$$\begin{aligned} & \frac{\partial}{\partial t}(h_1 h_2 h_3 \rho V) + \frac{\partial}{\partial \xi}[h_2 h_3 (\rho V^2 + P)] + \frac{\partial}{\partial \eta}(h_1 h_3 \rho UV) \\ & - (\rho U^2 + P) h_3 \frac{\partial h_2}{\partial \xi} + \rho UV h_3 \frac{\partial h_1}{\partial \eta} - P h_2 \frac{\partial h_3}{\partial \xi} \\ & = \frac{\partial}{\partial \xi}(h_2 h_3 \tau_{11}) + \frac{\partial}{\partial \eta}(h_1 h_3 \tau_{21}) \\ & + \tau_{21} h_3 \frac{\partial h_1}{\partial \eta} - \tau_{22} h_3 \frac{\partial h_2}{\partial \xi} - \tau_{33} h_2 \frac{\partial h_3}{\partial \xi} \end{aligned} \quad (\text{A2b})$$

η -momentum equation -

$$\begin{aligned} & \frac{\partial}{\partial t}(h_1 h_2 h_3 \rho U) + \frac{\partial}{\partial \xi}(h_2 h_3 \rho UV) + \frac{\partial}{\partial \eta}[h_1 h_3 (\rho U^2 + P)] \\ & - P h_1 \frac{\partial h_3}{\partial \eta} + \rho UV h_3 \frac{\partial h_2}{\partial \xi} - (\rho V^2 + P) h_3 \frac{\partial h_1}{\partial \eta} \\ & = \frac{\partial}{\partial \xi}(h_2 h_3 \tau_{12}) + \frac{\partial}{\partial \eta}(h_3 h_1 \tau_{22}) \\ & + \tau_{12} h_3 \frac{\partial h_2}{\partial \xi} - \tau_{33} h_1 \frac{\partial h_3}{\partial \eta} - \tau_{11} h_3 \frac{\partial h_1}{\partial \eta} \end{aligned} \quad (\text{A2c})$$

Energy equation -

$$\begin{aligned}
 & \frac{\partial}{\partial t}(h_1 h_2 h_3 E) + \frac{\partial}{\partial \xi} [h_2 h_3 V(E + P)] + \frac{\partial}{\partial \eta} [h_1 h_3 U(E + P)] \\
 &= \frac{\partial}{\partial \xi} \left(\frac{h_2 h_3}{h_1} \kappa \frac{\partial T}{\partial \xi} \right) + \frac{\partial}{\partial \eta} \left(\frac{h_1 h_3}{h_2} \kappa \frac{\partial T}{\partial \eta} \right) \\
 &+ \frac{\partial}{\partial \xi} [h_2 h_3 (V\tau_{11} + U\tau_{12})] + \frac{\partial}{\partial \eta} [h_1 h_3 (V\tau_{12} + U\tau_{22})]
 \end{aligned} \tag{A2d}$$

Stress terms -

$$\begin{aligned}
 \tau_{11} &= 2\mu \left(\frac{1}{h_1} \frac{\partial V}{\partial \xi} + \frac{U}{h_1 h_2} \frac{\partial h_1}{\partial \eta} \right) + \lambda \nabla \cdot \vec{v} \\
 \text{and} \\
 \lambda \nabla \cdot \vec{v} &= - \frac{2\mu}{3h_1 h_2 h_3} \left[\frac{\partial}{\partial \xi} (h_2 h_3 V) + \frac{\partial}{\partial \eta} (h_1 h_3 U) \right] \\
 \tau_{22} &= 2\mu \left(\frac{1}{h_2} \frac{\partial U}{\partial \eta} + \frac{V}{h_1 h_2} \frac{\partial h_1}{\partial \xi} \right) + \lambda \nabla \cdot \vec{v} \\
 \tau_{33} &= 2\mu \left(\frac{V}{h_3 h_1} \frac{\partial h_3}{\partial \xi} + \frac{U}{h_2 h_3} \frac{\partial h_3}{\partial \eta} \right) + \lambda \nabla \cdot \vec{v} \\
 \tau_{23} &= 0 \\
 \tau_{13} &= 0 \\
 \tau_{12} &= \mu \left[\frac{h_2}{h_1} \frac{\partial}{\partial \xi} \left(\frac{U}{h_2} \right) + \frac{h_1}{h_2} \frac{\partial}{\partial \eta} \left(\frac{V}{h_1} \right) \right]
 \end{aligned} \tag{A2e}$$

When the coinvariant velocities

$$\begin{aligned}
 & u = hU \\
 \text{and} \\
 & v = hV
 \end{aligned} \tag{A3}$$

are introduced into the equations (A2), the result is as follows:

Continuity equation -

$$\frac{\partial}{\partial t}(h^2\rho) = -(\rho v)_\xi - (\rho u)_\eta - \rho\left(\frac{u}{\eta} + \frac{v}{\xi}\right) \quad (\text{A4a})$$

ξ -momentum equation -

$$\begin{aligned} \frac{\partial}{\partial t}(h^2\rho v) = & -\frac{\partial}{\partial \xi}(\rho v^2 + h^2P) - \frac{\partial}{\partial \eta}(\rho uv) + [2h^2P + \rho(u^2 + v^2)]\frac{\xi}{h^2} \\ & - \rho v\left(\frac{u}{\eta} + \frac{v}{\xi}\right) + \frac{h}{\xi\eta}\left[h\left(\frac{\partial}{\partial \xi}\tau_{11} + \frac{\partial}{\partial \eta}\tau_{21}\right)\right. \\ & \left. + \left(\frac{\xi^2 + h^2}{\xi h}\right)\tau_{11} + \left(\frac{h^2 + 2\eta^2}{\eta h}\right)\tau_{21} - \frac{\xi}{h}\tau_{22} - \frac{h}{\xi}\tau_{33}\right] \end{aligned} \quad (\text{A4b})$$

η -momentum equation -

$$\begin{aligned} \frac{\partial}{\partial t}(h^2\rho u) = & -\frac{\partial}{\partial \xi}(\rho uv) - \frac{\partial}{\partial \eta}(\rho u^2 + h^2P) + [2h^2P + \rho(u^2 + v^2)]\frac{\eta}{h^2} \\ & - \rho u\left(\frac{u}{\eta} + \frac{v}{\xi}\right) + \frac{h}{\xi\eta}\left[\left(\frac{\partial\tau_{12}}{\partial \xi} + \frac{\partial\tau_{22}}{\partial \eta}\right) + \left(\frac{2\xi^2 + h^2}{\xi h}\right)\tau_{12}\right. \\ & \left. + \left(\frac{\eta^2 + h^2}{\eta h}\right)\tau_{22} - \frac{h}{\eta}\tau_{33} - \frac{\eta}{h}\tau_{11}\right] \end{aligned} \quad (\text{A4c})$$

Energy equation -

$$\begin{aligned} \frac{\partial}{\partial t}(h^2E) = & -\frac{\partial}{\partial \xi}[v(E + P)] - \frac{\partial}{\partial \eta}[u(E + P)] - (E + P)\left(\frac{u}{\eta} + \frac{v}{\xi}\right) \\ & + \frac{\partial}{\partial \xi}\left(K\frac{\partial T}{\partial \xi}\right) + \frac{\partial}{\partial \eta}\left(K\frac{\partial T}{\partial \eta}\right) + K\left(\frac{1}{\xi}\frac{\partial T}{\partial \xi} + \frac{1}{\eta}\frac{\partial T}{\partial \eta}\right) + \frac{1}{\xi}(v\tau_{11} + u\tau_{12}) \\ & + \frac{1}{\eta}(v\tau_{12} + u\tau_{22}) + \frac{\partial}{\partial \xi}(v\tau_{11} + u\tau_{12}) + \frac{\partial}{\partial \eta}(v\tau_{12} + u\tau_{22}) \end{aligned} \quad (\text{A4d})$$

Stress terms -

$$\tau_{11} = \frac{2\mu}{h^4} \left(h^2 \frac{\partial v}{\partial \xi} - v\xi + u\eta \right) + \lambda \nabla \cdot \vec{V}$$

and

$$\lambda \nabla \cdot \vec{V} = - \frac{2\mu}{3h^2} \left(\frac{\partial v}{\partial \xi} + \frac{v}{\xi} + \frac{\partial u}{\partial \eta} + \frac{u}{\eta} \right)$$

$$\tau_{22} = \frac{2\mu}{h^4} \left(h^2 \frac{\partial u}{\partial \eta} - u\eta + v\xi \right) + \lambda \nabla \cdot \vec{V}$$

$$\tau_{33} = \frac{2\mu}{h^2} \left(\frac{v}{\xi} + \frac{u}{\eta} \right) + \lambda \nabla \cdot \vec{V}$$

$$\tau_{23} = 0$$

$$\tau_{13} = 0$$

$$\tau_{12} = \frac{\mu}{h^4} \left[h^2 \left(\frac{\partial u}{\partial \xi} + \frac{\partial v}{\partial \eta} \right) - 2(\xi u + \eta v) \right]$$

(A4e)

Explicit differentiation of product terms involving the metric h_3 has been avoided through differentiation by parts, that is,

$$\frac{\partial \phi h_3}{\partial \omega} = h_3 \frac{\partial \phi}{\partial \omega} + \phi \frac{\partial h_3}{\partial \omega}$$

For any function ϕ where $h_3 = h_3(\omega)$, the term $\partial h_3 / \partial \omega$ is evaluated analytically.

Equations (A4) are singular along the lines $\xi = 0$ and $\eta = 0$ and have corresponding velocities $v = 0$ and $u = 0$. To obtain the equations valid along these two lines, it is necessary to differentiate equations (A4) with respect to each of the singular coordinates, and then take the limits, $\xi \rightarrow 0$ and $\eta \rightarrow 0$, as appropriate. The resulting equations are listed below:

Limiting form of equation along $\xi = 0$.

Continuity equation -

$$\frac{\partial}{\partial t} (h^2 \rho) = -2 \frac{\partial}{\partial \xi} (\rho v) - \frac{\partial}{\partial \eta} (\rho u) - \frac{\rho u}{\eta} \quad (\text{A5a})$$

ξ -momentum equation -

$$\mathbf{v} = 0 \quad (\text{A5b})$$

η -momentum equation -

$$\begin{aligned} \frac{\partial}{\partial t}(h^2 \rho u) &= -2 \frac{\partial}{\partial \xi}(\rho u v) - \frac{\partial}{\partial \eta}(\rho u^2 + h^2 P) + (2h^2 P + \rho u^2) \frac{\eta}{h^2} - \rho u \left(\frac{u}{\eta} \right) \\ &+ h^2 \left[\frac{\partial \tau_{22}}{\partial \eta} + 2 \frac{\partial \tau_{12}}{\partial \xi} + \frac{1}{\eta}(\tau_{22} - \tau_{33}) \right] + \eta(\tau_{22} - \tau_{11}) + 3\xi \tau_{12} \end{aligned} \quad (\text{A5c})$$

Energy equation -

$$\begin{aligned} \frac{\partial}{\partial t}(h^2 E) &= -2 \frac{\partial}{\partial \xi} [v(E + P)] - \frac{\partial}{\partial \eta} [u(E + P)] - (E + P) \left(\frac{u}{\eta} \right) \\ &+ 2 \frac{\partial}{\partial \xi} \left(\kappa \frac{\partial T}{\partial \xi} \right) + \frac{\partial}{\partial \eta} \left(\kappa \frac{\partial T}{\partial \eta} \right) + \frac{\kappa}{\eta} \frac{\partial T}{\partial \eta} + 2 \frac{\partial}{\partial \xi} (v \tau_{11} + u \tau_{12}) \\ &+ \frac{\partial}{\partial \eta} (v \tau_{12} + u \tau_{22}) + \frac{1}{\eta} (v \tau_{12} + u \tau_{22}) \end{aligned} \quad (\text{A5d})$$

Stress terms -

$$\left. \begin{aligned} \lambda \nabla \cdot \vec{v} &= \frac{-2\mu}{3h^2} \left(2 \frac{\partial v}{\partial \xi} + \frac{\partial u}{\partial \eta} + \frac{u}{\eta} \right) \\ \tau_{11} &= \frac{2\mu}{h^4} \left(h^2 \frac{\partial v}{\partial \xi} - \xi v + \eta u \right) + \lambda \nabla \cdot \vec{v} \\ \tau_{22} &= \frac{2\mu}{h^4} \left(h^2 \frac{\partial u}{\partial \eta} - \eta u + v \xi \right) + \lambda \nabla \cdot \vec{v} \\ \tau_{33} &= \frac{2\mu}{h^4} \left[h^2 \left(\frac{\partial v}{\partial \xi} + \frac{u}{\eta} \right) - 2v \xi \right] + \lambda \nabla \cdot \vec{v} \\ \tau_{23} &= 0 \\ \tau_{13} &= 0 \\ \tau_{12} &= \frac{\mu}{h^4} \left[h^2 \left(\frac{\partial u}{\partial \xi} + \frac{\partial v}{\partial \eta} \right) - 2\xi u \right] \end{aligned} \right\} \quad (\text{A5e})$$

APPENDIX A

Limiting form of equations along $\eta = 0$.

Continuity equation -

$$\frac{\partial}{\partial t}(h^2\rho) = - \frac{\partial}{\partial \xi}(\rho v) - 2 \frac{\partial}{\partial \eta}(\rho u) - \rho \left(\frac{v}{\xi} \right) \quad (\text{A6a})$$

ξ -momentum equation -

$$\begin{aligned} \frac{\partial}{\partial t}(h^2\rho v) = & - \frac{\partial}{\partial \xi}(\rho v^2 + h^2 P) - 2 \frac{\partial}{\partial \eta}(\rho uv) + (2h^2 P + \rho v^2) \frac{\xi}{h^2} - \rho v \left(\frac{v}{\xi} \right) \\ & + h^2 \left[\frac{\partial \tau_{11}}{\partial \xi} + 2 \frac{\partial \tau_{21}}{\partial \eta} + \frac{1}{\xi}(\tau_{11} - \tau_{33}) \right] + \xi(\tau_{11} - \tau_{22}) + 3\eta\tau_{21} \end{aligned} \quad (\text{A6b})$$

η -momentum equation -

$$u = 0 \quad (\text{A6c})$$

Energy equation -

$$\begin{aligned} \frac{\partial (h^2 E)}{\partial t} = & - \frac{\partial}{\partial \xi} [v(E + P)] - 2 \frac{\partial}{\partial \eta} [u(E + P)] \\ & - (E + P) \left(\frac{v}{\xi} \right) + \frac{\partial}{\partial \xi} \left(K \frac{\partial T}{\partial \xi} \right) \\ & + 2 \frac{\partial}{\partial \eta} \left(K \frac{\partial T}{\partial \eta} \right) + \frac{\partial}{\partial \xi} (v\tau_{11} + u\tau_{12}) \\ & + \frac{1}{\xi} (v\tau_{11} + u\tau_{12}) + 2 \frac{\partial}{\partial \eta} (v\tau_{12} + u\tau_{22}) \end{aligned} \quad (\text{A6d})$$

Stress terms -

$$\left. \begin{aligned}
 \lambda \nabla \cdot \vec{v} &= -\frac{2\mu}{3h^2} \left(\frac{\partial v}{\partial \xi} + \frac{v}{\xi} + 2 \frac{\partial u}{\partial \eta} \right) \\
 \tau_{11} &= \frac{2\mu}{h^4} \left(h^2 \frac{\partial v}{\partial \xi} - \xi v + \eta u \right) + \lambda \nabla \cdot \vec{v} \\
 \tau_{22} &= \frac{2\mu}{h^4} \left(h^2 \frac{\partial u}{\partial \eta} - \eta u + \xi v \right) + \lambda \nabla \cdot \vec{v} \\
 \tau_{33} &= \frac{2\mu}{h^4} \left[h^2 \left(\frac{\partial u}{\partial \eta} + \frac{v}{\xi} \right) - 2u\eta \right] + \lambda \nabla \cdot \vec{v} \\
 \tau_{23} &= 0 \\
 \tau_{13} &= 0 \\
 \tau_{12} &= \frac{\mu}{h^4} \left[h^2 \left(\frac{\partial u}{\partial \xi} + \frac{\partial v}{\partial \eta} \right) - 2\eta v \right]
 \end{aligned} \right\} \quad (A6e)$$

The previous dimensional equations are nondimensionalized as follows:

$$\begin{aligned}
 \rho &= \frac{\hat{\rho}}{\hat{\rho}_\infty} & u &= \frac{\hat{u}}{\hat{u}_\infty \hat{L}^{1/2}} & v &= \frac{\hat{v}}{\hat{u}_\infty \hat{L}^{1/2}} \\
 P &= \frac{\hat{P}}{\hat{\rho}_\infty \hat{u}_\infty^2} & e &= \frac{\hat{e}}{\hat{c}_v \hat{T}_\infty} & \xi &= \frac{\hat{\xi}}{\hat{L}^{1/2}} \\
 \eta &= \frac{\hat{\eta}}{\hat{L}^{1/2}} & \mu &= \frac{\hat{\mu}}{\hat{\mu}_\infty} & K &= \frac{\hat{K}}{\hat{K}_\infty} & t &= \frac{\hat{t}_\infty \hat{u}_\infty}{\hat{L}}
 \end{aligned}$$

The components of the vector expression

$$\frac{\partial \vec{W}}{\partial t} = -\frac{\partial \vec{F}(W)}{\partial \xi} - \frac{\partial \vec{G}(W)}{\partial \eta} + \vec{H}(W) + \vec{S}(W)$$

can now be written as follows:

$$\left. \begin{aligned}
 \vec{W} &= \begin{bmatrix} h^2 \rho \\ h^2 \rho v \\ h^2 \rho u \\ h^2 E \end{bmatrix} & \vec{F} &= \begin{bmatrix} \rho v \\ \rho v^2 + h^2 P \\ \rho uv \\ v(E + C_2 P) \end{bmatrix} \\
 \vec{G} &= \begin{bmatrix} \rho u \\ \rho uv \\ \rho u^2 + h^2 P \\ u(E + C_2 P) \end{bmatrix} & \vec{H} &= \begin{bmatrix} -\rho \left(\frac{u}{\eta} + \frac{v}{\xi} \right) \\ \left[2h^2 P + \rho(u^2 + v^2) \right] \frac{\xi}{h^2} - \rho v \left(\frac{u}{\eta} + \frac{v}{\xi} \right) \\ \left[2h^2 P + \rho(u^2 + v^2) \right] \frac{\eta}{h^2} - \rho u \left(\frac{u}{\eta} + \frac{v}{\xi} \right) \\ -(E + C_2 P) \left(\frac{u}{\eta} + \frac{v}{\xi} \right) \end{bmatrix}
 \end{aligned} \right\} \quad (A7)$$

where $E = \rho[e + C_1(u^2 + v^2)]$ and

$$\vec{S} = \frac{1}{N_{Re_\infty}} \begin{bmatrix} 0 \\ \frac{h}{\xi \eta} \left[h \left(\frac{\partial \tau_{11}}{\partial \xi} + \frac{\partial}{\partial \eta} \tau_{21} \right) + \left(\frac{\xi^2 + h^2}{\xi h} \right) \tau_{11} + \left(\frac{h^2 + 2\eta^2}{\eta h} \right) \tau_{21} - \frac{\xi}{h} \tau_{22} - \frac{h}{\xi} \tau_{33} \right] \\ \frac{h}{\xi \eta} \left[h \left(\frac{\partial \tau_{12}}{\partial \xi} + \frac{\partial \tau_{22}}{\partial \eta} \right) + \left(\frac{2\xi^2 + h^2}{\xi h} \right) \tau_{12} + \left(\frac{\eta^2 + h^2}{\eta h} \right) \tau_{22} - \frac{h}{\eta} \tau_{33} - \frac{\eta}{h} \tau_{11} \right] \\ \frac{C_2 \gamma}{N_{Pr_\infty}} \left[\frac{\partial}{\partial \xi} \left(\kappa \frac{\partial T}{\partial \xi} \right) + \frac{\partial}{\partial \eta} \left(\kappa \frac{\partial T}{\partial \eta} \right) + \kappa \left(\frac{1}{\xi} \frac{\partial T}{\partial \xi} + \frac{1}{\eta} \frac{\partial T}{\partial \eta} \right) \right] \\ + \frac{1}{\xi} (v \tau_{11} + u \tau_{12}) + \frac{1}{\eta} (v \tau_{12} + u \tau_{22}) \\ + \frac{\partial}{\partial \xi} (v \tau_{11} + u \tau_{12}) + \frac{\partial}{\partial \eta} (v \tau_{12} + u \tau_{22}) \end{bmatrix}$$

APPENDIX A

The \vec{W} , \vec{F} , and \vec{G} terms remain unchanged along the lines $\xi = 0$ and $\eta = 0$. However, the \vec{H} and \vec{S} terms are redefined as follows:

$$\vec{H} = \begin{bmatrix} -\frac{\partial(\rho v)}{\partial \xi} - \frac{\rho u}{\eta} \\ 0 \\ (2h^2 P + \rho u^2) \frac{\eta}{h^2} - \rho u \left(\frac{u}{\eta} \right) - \frac{\partial(\rho uv)}{\partial \xi} \\ -\frac{\partial}{\partial \xi} [v(E + C_2 P)] - (E + C_2 P) \left(\frac{u}{\eta} \right) \end{bmatrix} \quad \text{for } \xi = 0$$

$$\vec{H} = \begin{bmatrix} -\frac{\partial(\rho u)}{\partial \eta} - \frac{\rho v}{\xi} \\ (2h^2 P + \rho v^2) \frac{\xi}{h^2} - \rho v \left(\frac{v}{\xi} \right) - \frac{\partial}{\partial \eta} (\rho uv) \\ 0 \\ -(E + C_2 P) \left(\frac{v}{\xi} \right) - \frac{\partial}{\partial \eta} u(E + C_2 P) \end{bmatrix} \quad \text{for } \eta = 0$$

$$\vec{S} = \frac{1}{N_{Re_\infty}} \begin{bmatrix} 0 \\ 0 \\ h^2 \left[\frac{\partial \tau_{22}}{\partial \eta} + 2 \frac{\partial \tau_{12}}{\partial \xi} + \frac{1}{\eta} (\tau_{22} - \tau_{33}) \right] + \eta (\tau_{22} - \tau_{11}) + 3\xi \tau_{12} \\ \frac{C_2 \gamma}{N_{Pr_\infty}} \left[2 \frac{\partial}{\partial \xi} \left(\kappa \frac{\partial T}{\partial \eta} \right) + \frac{\partial}{\partial \eta} \left(\kappa \frac{\partial T}{\partial \eta} \right) + \frac{\kappa}{\eta} \frac{\partial T}{\partial \eta} \right] \\ + 2 \frac{\partial}{\partial \xi} (v \tau_{11} + u \tau_{12}) \\ + \frac{\partial}{\partial \eta} (v \tau_{12} + u \tau_{22}) + \frac{1}{\eta} (v \tau_{12} + u \tau_{22}) \end{bmatrix} \quad \text{for } \xi = 0$$

APPENDIX A

$$\vec{s} = \frac{1}{N_{Re_\infty}} \begin{bmatrix} 0 \\ h^2 \left[\frac{\partial \tau_{11}}{\partial \xi} + 2 \frac{\partial \tau_{21}}{\partial \eta} + \frac{1}{\xi} (\tau_{11} - \tau_{33}) \right] \\ + \xi (\tau_{11} - \tau_{22}) + 3\eta \tau_{21} \\ 0 \\ \frac{C_2 \gamma}{N_{Pr_\infty}} \left[\frac{\partial}{\partial \xi} \left(\kappa \frac{\partial T}{\partial \xi} \right) + 2 \frac{\partial}{\partial \eta} \left(\kappa \frac{\partial T}{\partial \eta} \right) + \frac{\kappa}{\xi} \frac{\partial T}{\partial \xi} \right] \\ + \frac{\partial}{\partial \xi} (v\tau_{11} + u\tau_{12}) + \frac{1}{\xi} (v\tau_{11} + u\tau_{12}) \\ + 2 \frac{\partial}{\partial \eta} (v\tau_{12} + u\tau_{22}) \end{bmatrix} \quad \text{for } \eta = 0$$

APPENDIX B

TRANSFORMATION OF INVISCID EQUATIONS

The conservative, vector form of the Euler equations, written in orthogonal parabolic coordinates (ξ, η, t) , was given by equation (12) as

$$\vec{W}_t = -\vec{F}_\xi(W) - \vec{G}_\eta(W) + \vec{H}(W)$$

where \vec{W} , \vec{F} , \vec{G} , and \vec{H} are vector quantities defined in appendix A. By using the transformation equations (3)

$$\bar{\xi} = \xi$$

$$\bar{\eta} = \frac{\eta - \eta_c}{\eta_s(\xi, t) - \eta_c}$$

$$\bar{t} = t$$

equation (12) can be transformed from parabolic coordinates (ξ, η, t) to a set of coordinates in computational space $(\bar{\xi}, \bar{\eta}, \bar{t})$. To carry out this transformation, the following transformation operators are defined:

$$\frac{\partial}{\partial \xi} = \frac{\partial \bar{\xi}}{\partial \xi} \frac{\partial}{\partial \bar{\xi}} + \frac{\partial \bar{\eta}}{\partial \xi} \frac{\partial}{\partial \bar{\eta}} + \frac{\partial \bar{t}}{\partial \xi} \frac{\partial}{\partial \bar{t}} \quad (\text{B1})$$

$$\frac{\partial}{\partial \eta} = \frac{\partial \bar{\xi}}{\partial \eta} \frac{\partial}{\partial \bar{\xi}} + \frac{\partial \bar{\eta}}{\partial \eta} \frac{\partial}{\partial \bar{\eta}} + \frac{\partial \bar{t}}{\partial \eta} \frac{\partial}{\partial \bar{t}} \quad (\text{B2})$$

$$\frac{\partial}{\partial t} = \frac{\partial \bar{\xi}}{\partial t} \frac{\partial}{\partial \bar{\xi}} + \frac{\partial \bar{\eta}}{\partial t} \frac{\partial}{\partial \bar{\eta}} + \frac{\partial \bar{t}}{\partial t} \frac{\partial}{\partial \bar{t}} \quad (\text{B3})$$

By using the transformation equations (eqs. (3)), equations (B1) to (B3) can be written as follows:

$$\frac{\partial}{\partial \xi} = \frac{\partial}{\partial \bar{\xi}} + \frac{\partial \bar{\eta}}{\partial \xi} \frac{\partial}{\partial \bar{\eta}} \quad (\text{B4})$$

$$\frac{\partial}{\partial \eta} = \frac{\partial \bar{\eta}}{\partial \eta} \frac{\partial}{\partial \bar{\eta}} \quad (\text{B5})$$

APPENDIX B

$$\frac{\partial}{\partial t} = \frac{\partial \bar{\eta}}{\partial t} \frac{\partial}{\partial \bar{\eta}} + \frac{\partial}{\partial \bar{t}} \quad (\text{B6})$$

where

$$\frac{\partial \bar{\eta}}{\partial \xi} = - \left(\frac{\bar{\eta}}{\eta_s - \eta_c} \right) \frac{\partial \eta_s}{\partial \xi} \quad (\text{B7})$$

$$\frac{\partial \bar{\eta}}{\partial \eta} = \frac{1}{\eta_s - \eta_c} \quad (\text{B8})$$

$$\frac{\partial \bar{\eta}}{\partial t} = - \left(\frac{\bar{\eta}}{\eta_s - \eta_c} \right) \frac{\partial \eta_s}{\partial t} \quad (\text{B9})$$

With the transformation operators defined by equations (B4) through (B6), the vector form of Euler's equation (eq. (12)), can be transformed to computational space and written as follows:

$$\vec{W}_{\bar{t}} = - \frac{\partial \bar{\eta}}{\partial t} \vec{W}_{\bar{\eta}} - \vec{F}_{\bar{\xi}} - \frac{\partial \bar{\eta}}{\partial \xi} \vec{F}_{\bar{\eta}} - \frac{\partial \bar{\eta}}{\partial \eta} \vec{G}_{\bar{\eta}} + \vec{H} \quad (\text{B10})$$

Since only steady-state solutions are of interest, the term $\partial \bar{\eta} / \partial t$ can be neglected since it approaches zero as the steady state is approached. Thus, the previous equation can be written as

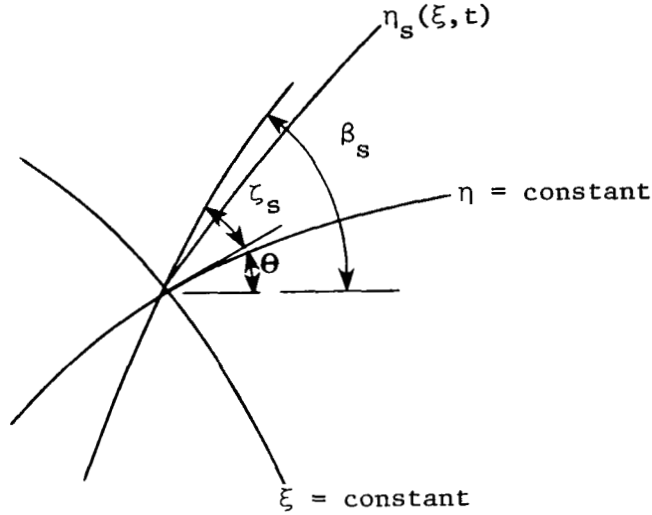
$$\vec{W}_{\bar{t}} = - \vec{F}_{\bar{\xi}} - \frac{\partial \bar{\eta}}{\partial \xi} \vec{F}_{\bar{\eta}} - \frac{\partial \bar{\eta}}{\partial \eta} \vec{G}_{\bar{\eta}} + \vec{H}$$

where $\partial \bar{\eta} / \partial \xi$ and $\partial \bar{\eta} / \partial \eta$ are defined by equations (B7) and (B8), respectively. This is the same as equation (14) presented in the main text.

APPENDIX C

CALCULATION OF PROPERTIES AT SHOCK WAVE

A method similar to that presented in reference 10 was the known pressure to calculate the shock velocity and other thermodynamic properties at the shock wave. Consider the shock wave illustrated in sketch (a) which can be expressed as $\eta_s = \eta_s(\xi, t)$:



Sketch (a)

The shock-wave angle β_s can be expressed as

$$\beta_s = \theta + \zeta_s \quad (C1)$$

where the slope θ of the coordinate line $\eta = \text{constant}$ and the deviation ζ_s of the shock wave from the coordinate line $\eta = \text{constant}$ are given by the following equations:

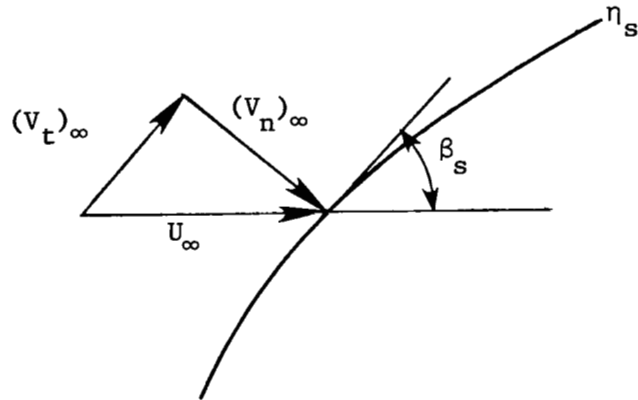
$$\theta = \tan^{-1} \left(\frac{\eta}{\xi} \right)_s \quad (C2)$$

$$\zeta_s = \tan^{-1} \left(\frac{\partial \eta_s}{\partial \xi} \right) \quad (C3)$$

The derivative $\partial \eta_s / \partial \xi$ is computed numerically using central differences at each time step except at the downstream boundary where three-point backward differences are used.

APPENDIX C

Now, consider the velocities on the upstream side of the shock wave illustrated in sketch (b):



Sketch (b)

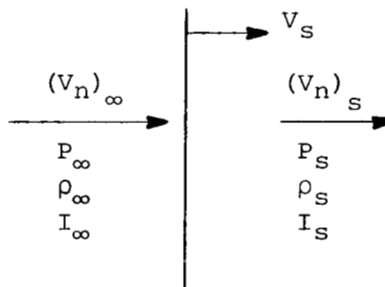
The tangential component of velocity $(V_t)_\infty$ is given by the equation

$$(V_t)_\infty = U_\infty \cos \beta_s \quad (C4)$$

and the normal component of velocity $(V_n)_\infty$ is given by the equation

$$(V_n)_\infty = U_\infty \sin \beta_s \quad (C5)$$

Changes across the shock wave can be related to the normal component, and the shock velocity illustrated by sketch (c):



Sketch (c)

Conditions across the shock wave can be related by the following normal shock-wave equations:

$$\rho_\infty [(V_n)_\infty - v_s] = \rho_s [(V_n)_s - v_s] \quad (C6)$$

APPENDIX C

$$P_{\infty} + \rho_{\infty} [(V_n)_{\infty} - v_s]^2 = P_s + \rho_s [(V_n)_s - v_s]^2 \quad (C7)$$

$$\frac{\gamma I_{\infty}}{C_2} + \frac{1}{2} [(V_n)_{\infty} - v_s]^2 = \frac{\gamma I_s}{C_2} + \frac{1}{2} [(V_n)_s - v_s]^2 \quad (C8)$$

or, since $\rho_{\infty} = 1$,

$$[(V_n)_{\infty} - v_s] = \rho_s [(V_n)_s - v_s] \quad (C9)$$

$$P_{\infty} + [(V_n)_{\infty} - v_s]^2 = P_s + \rho_s [(V_n)_s - v_s]^2 \quad (C10)$$

$$\frac{\gamma I_{\infty}}{C_2} + \frac{1}{2} [(V_n)_{\infty} - v_s]^2 = \frac{\gamma I_s}{C_2} + \frac{1}{2} [(V_n)_s - v_s]^2 \quad (C11)$$

Now, rearranging equation (C10) the following expression can be obtained:

$$P_s - P_{\infty} = [(V_n)_{\infty} - v_s]^2 \left\{ 1 - \rho_s \frac{[(V_n)_s - v_s]^2}{[(V_n)_{\infty} - v_s]^2} \right\} \quad (C12)$$

Combining this equation with equation (C9) and solving for $[(V_n)_{\infty} - v_s]^2$, the following is obtained:

$$[(V_n)_{\infty} - v_s]^2 = \frac{P_s - P_{\infty}}{1 - \frac{1}{\rho_s}} \quad (C13)$$

Similarly, equation (C11) becomes

$$\frac{\gamma I_s}{C_2} = \frac{\gamma I_{\infty}}{C_2} + \frac{1}{2} [(V_n)_{\infty} - v_s]^2 \left[1 - \left(\frac{1}{\rho_s} \right)^2 \right] \quad (C14)$$

Equations (C13) and (C14) can be combined with the ideal gas equation of state $P = \rho(\gamma - 1) \frac{I}{C_2}$ to yield the following result:

$$\frac{1}{\rho_s} = \left[\frac{\gamma \frac{I}{C_2} + \frac{1}{2}(P_s - P_{\infty})}{P_s \left(\frac{C_2}{\gamma - 1} \right) - \frac{1}{2}(P_s - P_{\infty})} \right] \quad (C15)$$

APPENDIX C

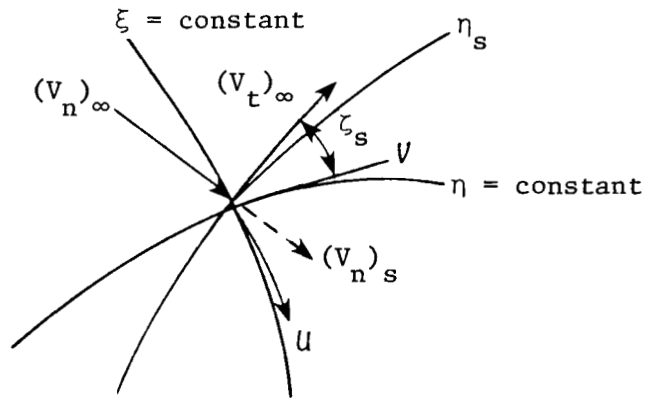
If the pressure on the downstream side of the shock wave is known, the density can be calculated from equation (C15) and the shock velocity can be calculated from the following equation:

$$V_s = (V_n)_\infty \sqrt{\frac{P_s - P_\infty}{1 - \frac{1}{\rho_s}}} \quad (C16)$$

The velocity components in the parabolic coordinate system can now be related to the velocity components normal and tangent to the shock wave by the following equations. (See sketch (d).)

$$u = -(V_n)_s \cos \zeta_s + (V_t)_\infty \sin \zeta_s \quad (C17)$$

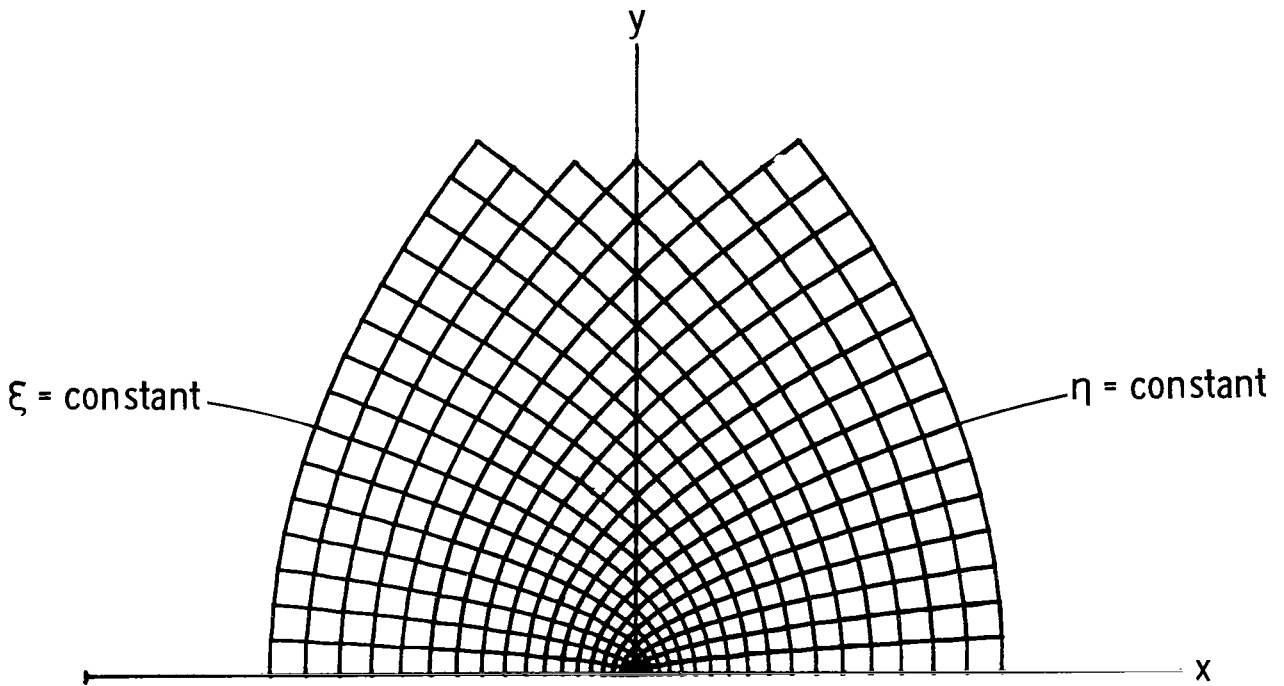
$$v = (V_n)_s \sin \zeta_s + (V_t)_\infty \cos \zeta_s \quad (C18)$$



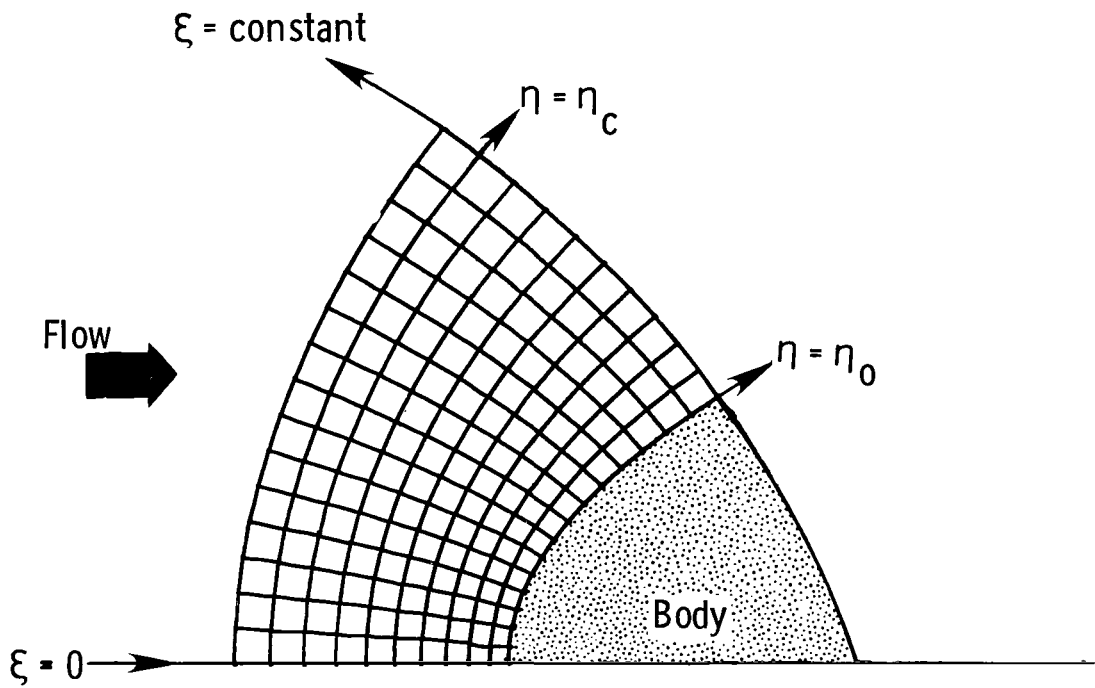
Sketch (d)

REFERENCES

1. Moretti, Gino; and Salas, Manuel D.: The Blunt Body Problem for a Viscous Rarefied Gas Flow. AIAA Paper No. 69-139, Jan. 1969.
2. Davis, R. T.: Numerical Solution of the Hypersonic Viscous Shock-Layer Equations. AIAA J., vol. 8, no. 5, May 1970, pp. 843-851.
3. Kumar, Ajay; and Graves, R. A., Jr.: Numerical Solution of the Viscous Hypersonic Flow Past Blunted Cones at Angle of Attack. AIAA Paper No. 77-172, Jan. 1977.
4. Peyret, Roger; and Viviand, Henri: Calculation of the Flow of a Viscous Compressible Fluid Around an Obstacle of Parabolic Shape. NASA TT F-16558, 1975.
5. Gnoffo, Peter A.: Forebody and Afterbody Solutions of the Navier-Stokes Equations for Supersonic Flow Over Blunt Bodies in a Generalized Orthogonal Coordinate System. NASA TP-1075, 1978.
6. Weilmuenster, K. James; and Howser, Lona M.: Solution of a Large Hydrodynamic Problem Using the STAR-100 Computer. NASA TM X-73904, 1976.
7. Blottner, F. G.: Variable Grid Scheme Applied to Turbulent Boundary Layers. Comput. Methods Appl. Mech. & Eng., vol. 4, no. 2, Sept. 1974, pp. 179-194.
8. Thommen, Hans U.: Numerical Integration of the Navier-Stokes Equations. Z. Angew. Math. & Phys., vol. 17, fasc. 3, 1966, pp. 369-384.
9. MacCormack, Robert W.: The Effect of Viscosity in Hypervelocity Impact Cratering. AIAA Paper No. 69-354, Apr.-May 1969.
10. Tannehill, J. C.; Holst, T. L.; and Rakich, J. V.: Numerical Computation of Two-Dimensional Viscous Blunt Body Flows With an Impinging Shock. AIAA Paper 75-154, Jan. 1975.
11. Little, Herbert R.: An Experimental Investigation of Surface Conditions on Hyperboloids and Paraboloids at a Mach Number of 10. AEDC-TR-69-225, U.S. Air Force, Jan. 1970. (Available from DDC as AD 698 755.)
12. Graves, Randolph Anderson, Jr.: Solutions to the Navier-Stokes Equations for Supersonic Flow Over Blunt Bodies With Massive Wall Blowing. Ph. D. Thesis, The George Washington Univ., 1977.
13. Anderson, E. C.; and Lewis, C. H.: Laminar or Turbulent Boundary-Layer Flows of Perfect Gases or Reacting Gas Mixtures in Chemical Equilibrium. NASA CR-1893, 1971.
14. Marconi, Frank; Yaeger, Larry; and Hamilton, H. Harris: Computation of High-Speed Inviscid Flows About Real Configurations. Aerodynamic Analyses Requiring Advanced Computers - Part II, NASA SP-347, 1975, pp. 1411-1455.

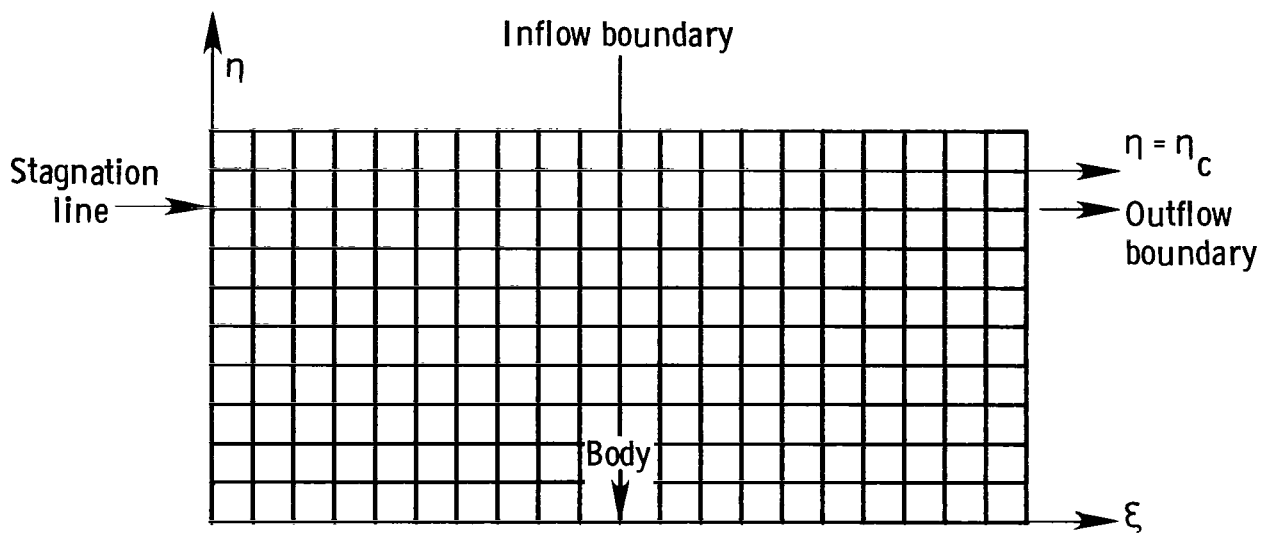


(a) Physical plane.

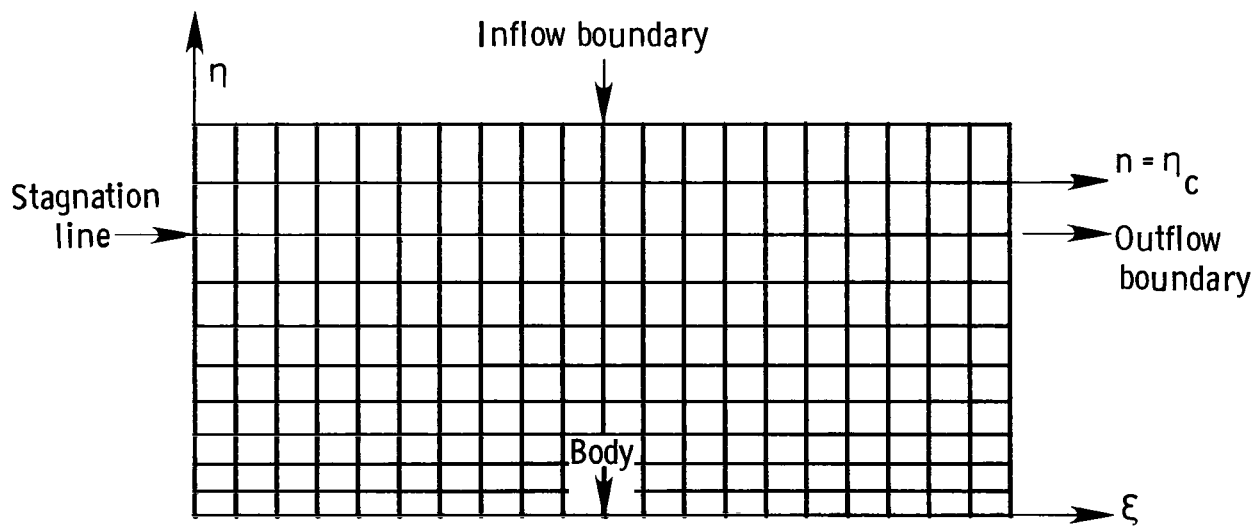


(b) Physical plane; viscous solution.

Figure 1.- Physical and computational planes for viscous solution.



(c) Computational plane; viscous solution.



(d) Physical plane with stretched viscous solution.

Figure 1.- Concluded.

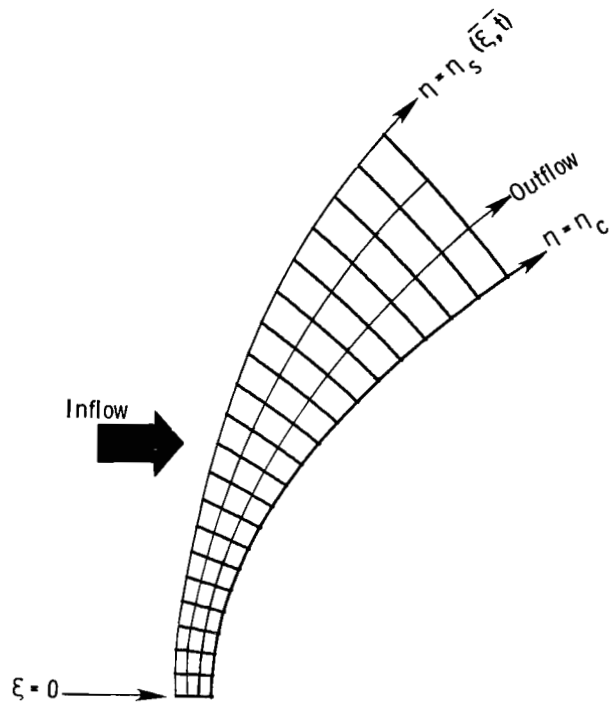


Figure 2.- Physical plane; inviscid solution.

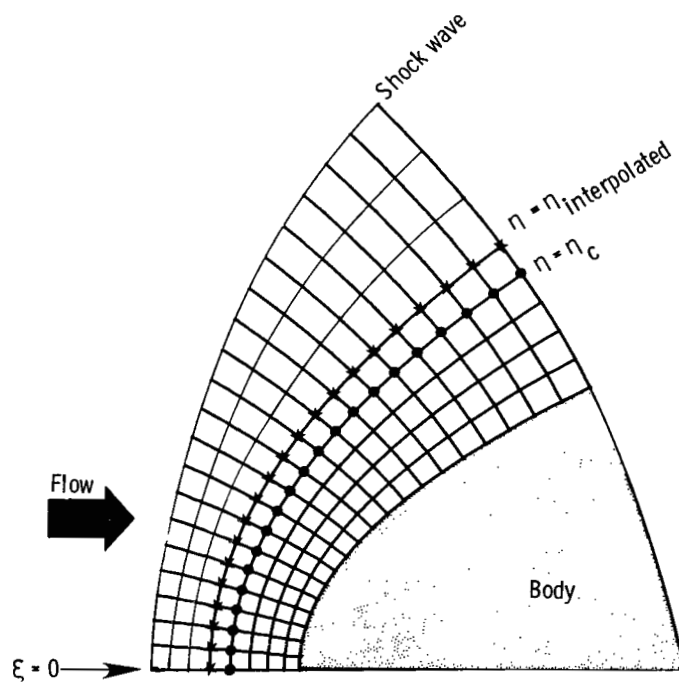


Figure 3.- Merged inner and outer solution grids.

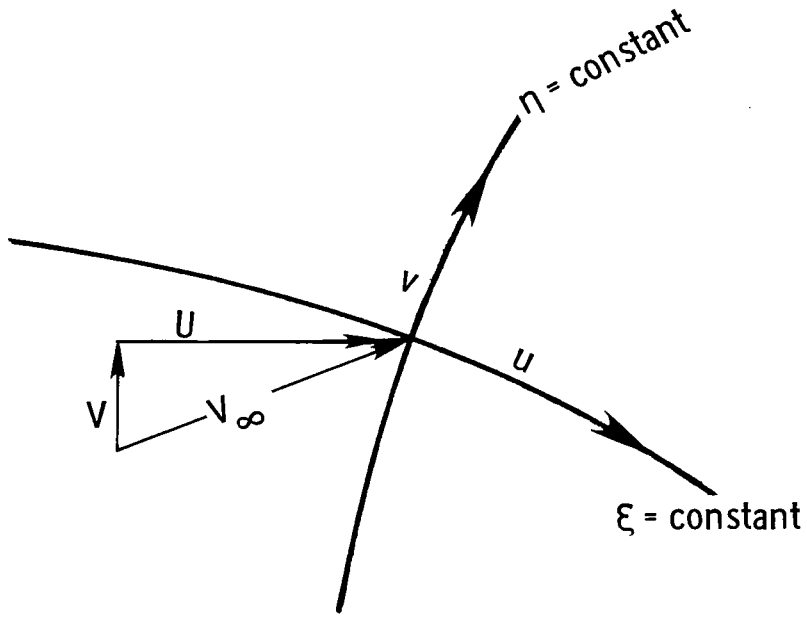


Figure 4.- Velocity field.

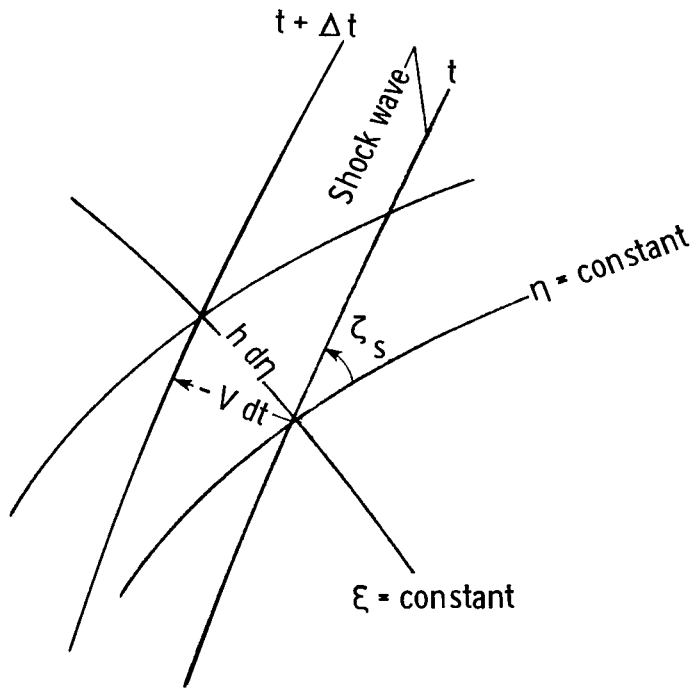


Figure 5.- Movement of shock wave.

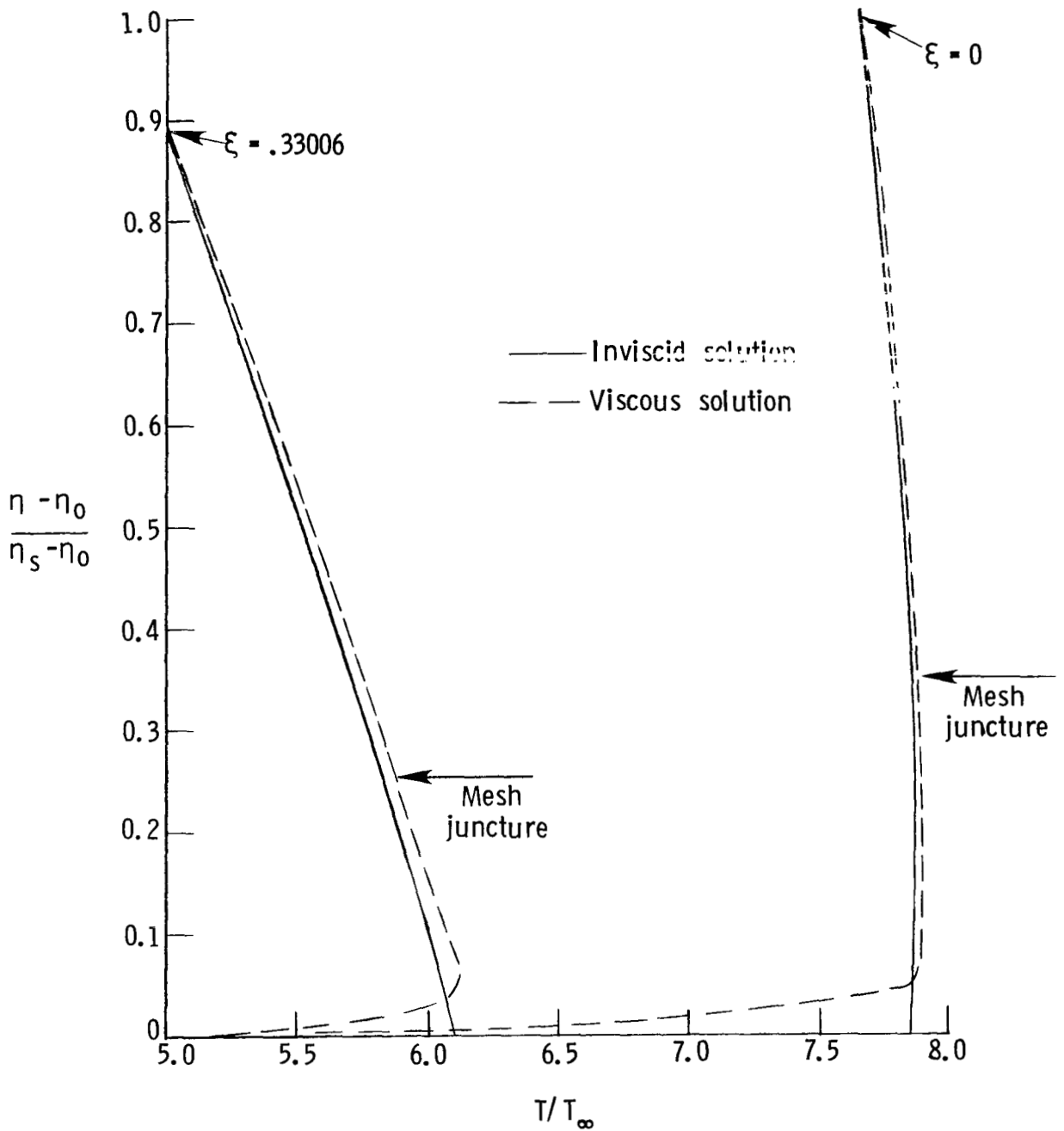


Figure 6.- Temperature distributions through shock layer for $N_{Re_\infty} = 2 \times 10^6$
 with $M_\infty = 5.8725$ and $T_w/T_\infty = 5.16$.

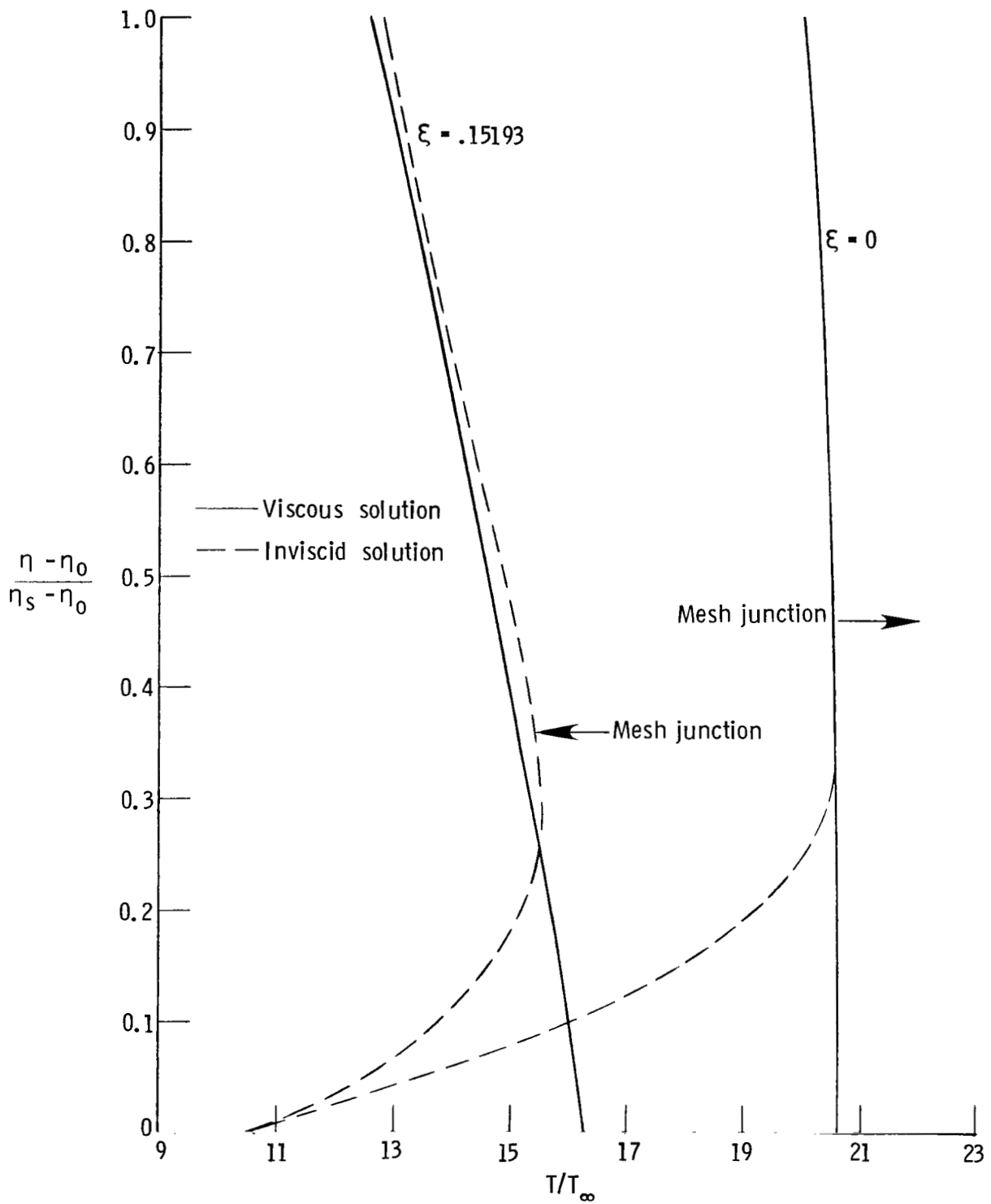


Figure 7.- Temperature distributions through shock layer for $N_{Re_\infty} = 3 \times 10^5$
 with $M_\infty = 9.92$ and $T_w/T_\infty = 10.36$.

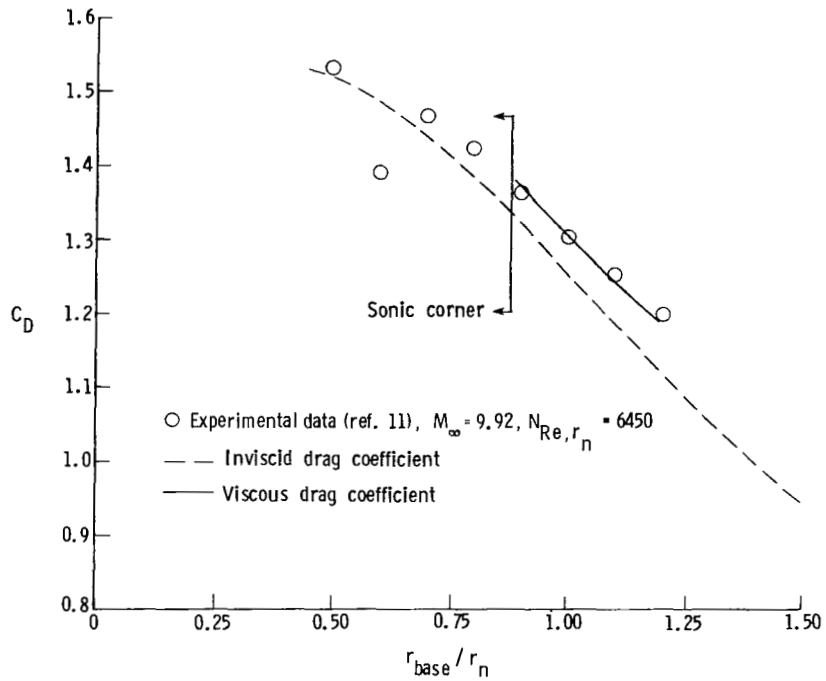


Figure 8.- Comparison of experimental and computed forebody drag coefficients C_D .

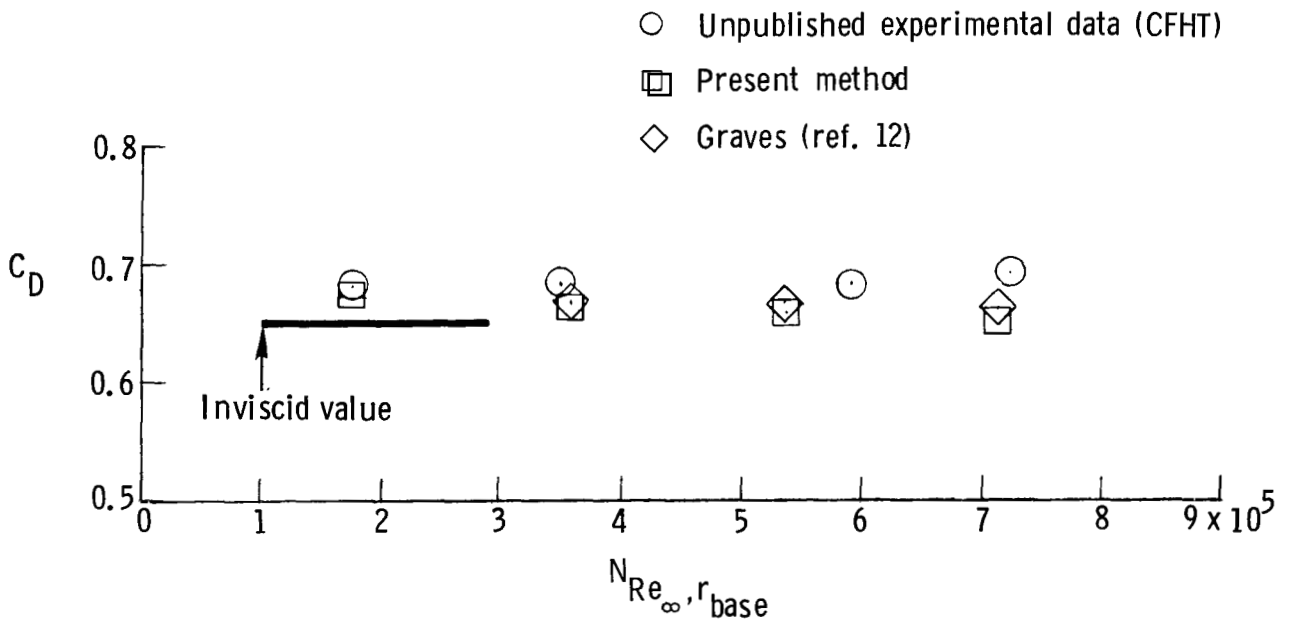


Figure 9.- Comparison of experimental and computed drag coefficients C_D at high Reynolds numbers.

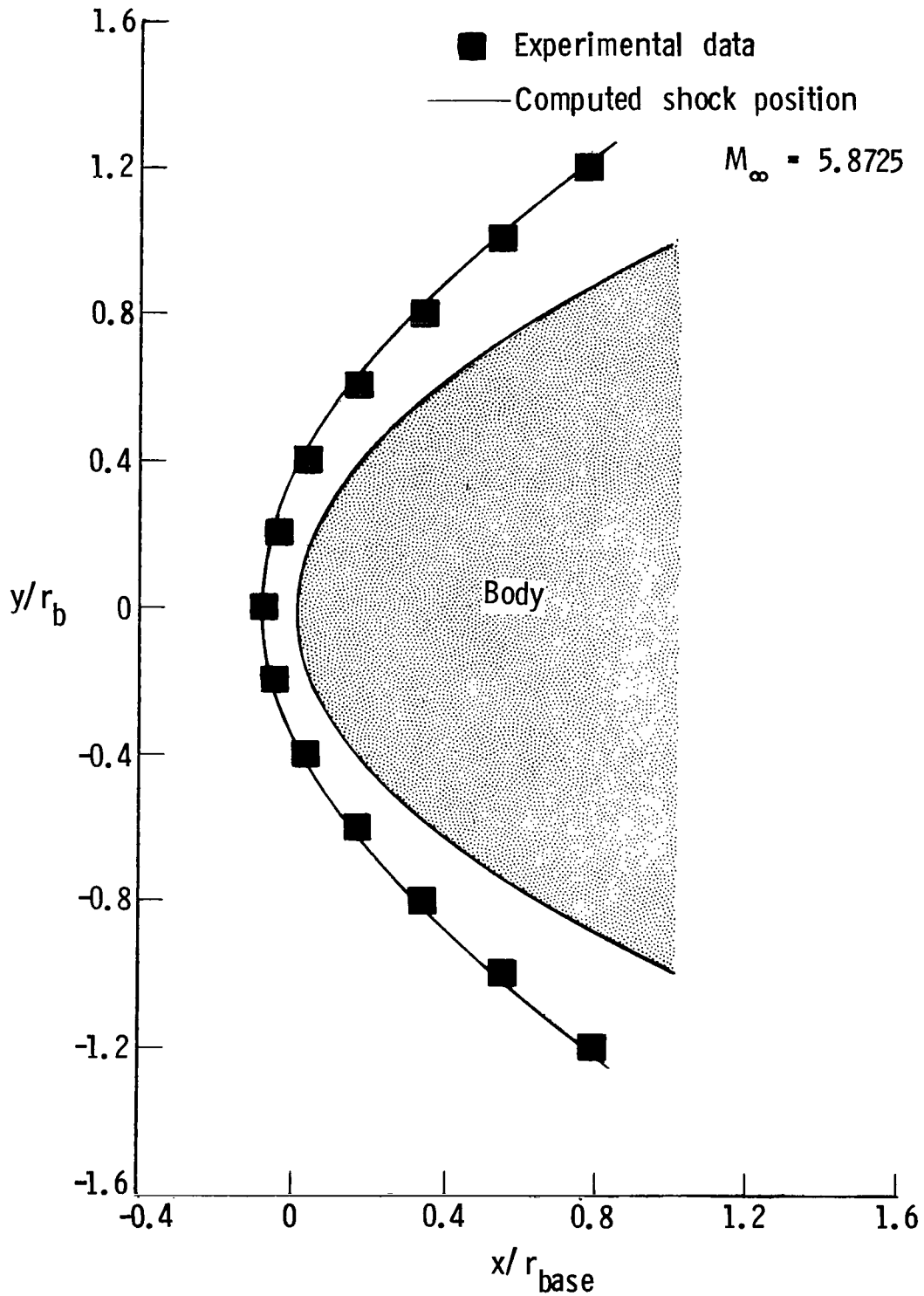


Figure 10.- Comparison of computed and experimental shock shape.

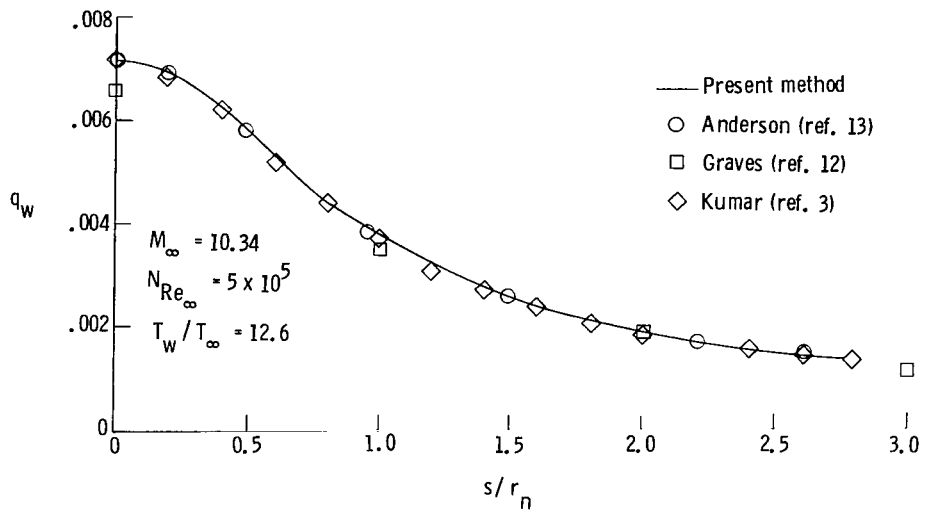


Figure 11.- Comparison of wall heat transfer determined by several different computational techniques.

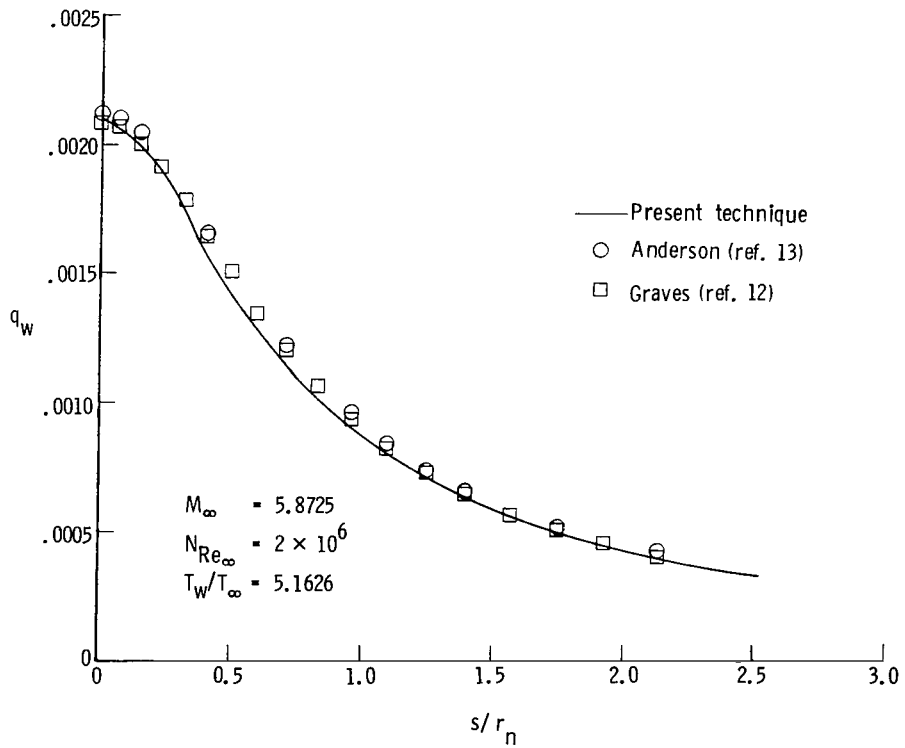


Figure 12.- Comparison of computed wall heat transfer.

1. Report No. NASA TP-1497		2. Government Accession No.		3. Recipient's Catalog No.	
4. Title and Subtitle A HYBRIDIZED METHOD FOR COMPUTING HIGH-REYNOLDS-NUMBER HYPERSONIC FLOW ABOUT BLUNT BODIES				5. Report Date October 1979	
				6. Performing Organization Code	
7. Author(s) K. James Weilmuenster and H. Harris Hamilton II				8. Performing Organization Report No. L-12946	
9. Performing Organization Name and Address NASA Langley Research Center Hampton, VA 23665				10. Work Unit No. 506-26-23-01	
				11. Contract or Grant No.	
12. Sponsoring Agency Name and Address National Aeronautics and Space Administration Washington, DC 20546				13. Type of Report and Period Covered Technical Paper	
				14. Sponsoring Agency Code	
15. Supplementary Notes					
16. Abstract A hybridized method for computing the flow about blunt bodies is presented. In this method the flow field is split into its viscid and inviscid parts. The forebody flow field about a parabolic body is computed. For the viscous solution, the Navier-Stokes equations are solved on orthogonal parabolic coordinates using explicit finite differencing. The inviscid flow is determined by using a "Moretti type" scheme in which the Euler equations are solved, using explicit finite differences, on a nonorthogonal coordinate system which uses the bow shock as an outer boundary. The two solutions are coupled along a common data line and are marched together in time until a converged solution is obtained. Computed results, when compared with experimental and analytical results, indicate the method works well over a wide range of Reynolds numbers and Mach numbers.					
17. Key Words (Suggested by Author(s)) Blunt body Viscous flows Finite difference			18. Distribution Statement Unclassified - Unlimited Subject Category 34		
19. Security Classif. (of this report) Unclassified		20. Security Classif. (of this page) Unclassified		21. No. of Pages 46	22. Price* \$4.50

* For sale by the National Technical Information Service, Springfield, Virginia 22161

NASA-Langley, 1979

National Aeronautics and
Space Administration

Washington, D.C.
20546

Official Business

Penalty for Private Use, \$300

THIRD-CLASS BULK RATE

Postage and Fees Paid
National Aeronautics and
Space Administration
NASA-451



2 1 1U,D, 092879 S00903DS
DEPT OF THE AIR FORCE
AF WEAPONS LABORATORY
ATTN: TECHNICAL LIBRARY (SUL)
KIRTLAND AFB NM 87117

NASA

POSTMASTER: If Undeliverable (Section 158
Postal Manual) Do Not Return